Study of the spectroscopic properties of Thulium doped in Yttrium Ytterbium Gallium Garnet (YYbGG) crystals

Geraldine Banda

Supervised by: Márcio A. R. C. Alencar
Federal University of Sergipe, Brazil

January 2026

DISSERTATION PRESENTED TO THE GRADUATE PROGRAM OF PHYSICS AT THE FEDERAL UNIVERSITY OF SERGIPE IN PARTIAL FULFILMENT OF THE REQUIREMENTS FOR THE AWARD OF MASTER OF SCIENCE IN CONDENSED MATTER PHYSICS

DECLARATION

This work was carried out at the Federal University of Sergipe (UFS) in fulfillment of the requirements for a Master's degree in condensed matter physics.

I hereby declare that except where due acknowledgment is made, this work has never been presented wholly or in part for the award of a degree at the Federal University of Sergipe (UFS) or any other University.

ACKNOWLEDGEMENTS

The successful completion of this research project is a result of the numerous contributions of many people. Their assistance, guidance, encouragement, and support have not escaped their attention. To all these people I say, I owe you a debt of gratitude, and although it is not possible to enumerate all their names here, I want them to know that I wholeheartedly appreciate their contributions.

I am deeply grateful to my supervisor Professor Márcio A. R. C. Alencar, and my lab partner, Lauro Espíndola for great supervision and guidance throughout this research which will remain a valuable lesson for my future research endeavors. Their involvement, patience, and true dedication to this project have been of tremendous value to me and I have acquired a lot of research skills through them.

DEDICATION

To my family and friends for the support rendered to the success of this project.

Abstract

Rare earth elements have been extensively investigated owing to their unique optical properties, which arise from intra-4f electronic transitions and are strongly influenced by both the dopant ion and the host crystal matrix. Among these materials, thulium-doped yttrium ytterbium gallium garnet (Tm:YYbGG) has attracted attention due to its potential for multifunctional luminescent applications. In this study, Tm:YYbGG crystals synthesised via a nucleation and growth process were systematically investigated to evaluate their spectroscopic and thermometric properties.

Under excitation at 800 nm and 980 nm, the material exhibited both downconversion and upconversion luminescence, demonstrating emissions in the visible and near-infrared (NIR) spectral regions. Power-dependent measurements confirmed multiphoton processes under upconversion and down conversion excitation, while temperature-dependent studies were conducted over the range 303–373 K to assess thermometric performance. Six distinct emission bands were observed, including visible emissions at 485 nm (blue), 650 nm (red), and 685 nm (deep red), as well as NIR emissions at 1050 nm, 1450 nm, and 1650 nm.

The luminescence intensity ratio (LIR) technique was applied to transitions originating from non-thermally coupled levels to determine temperature sensitivity. The relative sensitivity values were found to range from 0.72 to 1.02 % K^{-1} under downconversion excitation and from 1.64 to 2.26 % K^{-1} under upconversion excitation. The enhanced sensitivity observed under upconversion excitation indicates improved thermometric performance.

These findings demonstrate that Tm:YYbGG crystals exhibit stable and efficient luminescence behaviour, highlighting their potential as promising candidates for optical temperature sensing applications

Keywords: Luminescence, upconversion, downconversion, energy transfer, thermometry, and infrared and visible range emissions.

Contents

List of Figures

List of Tables

1. Introduction

1.1 Background

In recent years, there has been a growing interest in small scale structured materials doped with rare-earth either nano or micro crystals in biophotonics and photonics. Rare earth-doped crystals have a broad range of applications in lasers, amplifiers, biological imaging systems, and optical thermometry (Eliseeva and Bünzli, 2011). Research in optical luminescence has increased over the years resulting in the development of efficient small scale phosphors, which play a vital role in the operation of sensitive photonic sensors (Brandão-Silva et al., 2018). One of the materials that can be used in the development of photonic sensors is thulium. According to JHA (Jha, 2014), thulium is the least abundant of the rare earth elements but is very valuable. It has two valencies: 2 and 3. Natural thulium (Tm) is a very stable isotope and is mostly used in ferrite materials which are best suited in acoustic-optic devices.

Furthermore, trivalent thulium (Tm^{3+}) ions are mostly used in several applications as they can emit light at several wavelengths in infrared (IR), visible light (VIS), and ultraviolet (UV) due to their energy level structure. Regardless of the host with which Tm^{3+} ionic crystals are doped, these crystals display large energy separations between the luminescent levels and cover a wide wavelength range (Strzepek et al., 2020). Additionally, Tm^{3+} ions have a long luminescence lifetime ranging in the few hundreds of μs to ms (Seshagiri et al., 2010).

Thulium is very useful in optical studies due to its wide emission peak, particularly its emission at 1.8 μm in infrared corresponding to the transitions from $^3F_4$ to the $^3H_6$ energy level. It is relatively less explored compared to erbium. However, emissions of Tm^{3+} are observed in both the visible (350-700 nm) and infrared (700-3000 nm)(Guillemot et al., 2022).

In addition to that Hernanández-Rodriguez et al (Hernández-Rodriguez et al., 2017) highlight that, Tm^{3+} ions show absorption and emission bands in the near-infrared biological windows. These biological windows are those infrared spectral regions where the transmission of light through human tissue is most effective. The biological windows are divided into three regions: the first biological window (I-BW), which ranges between 650 and 950 nm, the second window (II-BW) between 1000 and 1300 nm, and the third window (III-BW) between 1500 and 1750 nm.

Tm^{3+} doped materials exhibit either up-conversion photoluminescence or down-conversion photoluminescence, phenomena influenced by their high density and lower phonon energy. Up-conversion photoluminescence has many useful applications in renewable energy and biomedical imaging; it involves the combination of multiple low energy photons into higher energy photons. When excited by low energy, high wavelength light such as near-infrared, the upconversion crystals absorb multiple photons continuously, resulting in a series of energy level transitions. On the contrary, down-conversion photoluminescence involves the conversion of a single high energy photon into multiple lower-energy photons when excited by high energy, low wavelength light such as ultraviolet, this results in two or more photons (Zhang et al., 2024).

Both Upconversion and Downconversion properties can be modified based on the dopant con-

centration, excitation wavelength, and host crystal characteristics. According to Zhang et al., (Zhang et al., 2024), the luminescence intensity is significantly affected by the density of the phonons of the host crystal. Specifically, a lower phonon energy of the host crystal promotes an increase in intensity. Therefore, selecting a suitable host crystal is essential for achieving high efficiency.

Yttrium ytterbium gallium garnet (YYbGG) a micro-sized crystal synthesized through controlled nucleation and growth, is a particularly promising crystalline system. Rare earth gallium garnets are interesting host materials for technological applications because of their unique properties, namely chemical stability, mechanical resistance and specific optical and magnetic characteristics. In this host material, Y^{3+} and Yb^{3+} are part of the host matrix and Tm^{3+} is the dopant. This combination enables precise control over energy transfer and efficient conversion of near infrared photons (Albino et al., 2024).

One of the applications of optical luminescence is a technique known as luminescence thermometry or optical thermometry. This technique involves detecting temperature variations by monitoring the changes in selected spectroscopic parameters in response to temperature. Temperature-dependent photoluminescence analyses are performed to demonstrate the suitability of lanthanide materials in several applications, such as optical imaging for early cancer detection and treatment (Panda et al., 2025). Given that it is noninvasive and a real-time monitoring technique, luminescence thermometry can be used in environments that are inaccessible to other methods. It is effective over a wide temperature range and has potential applications in cryogenic, extremely high temperature, and harsh environments (Dramićanin, 2020).

As reported by Rajashree Panda et al (Panda et al., 2025), inorganic materials are doped with various lanthanide ions including thulium and are utilized in optical sensing because of their unique electronic structure, thermalization of states, and multicolor emission. Additionally, lanthanides possess thermally coupled levels, that is closely spaced excited electronic energy levels whose energy gap is separated by an energy difference of $\Delta E = 200 - 2000 cm^{-1}$. In these levels the thermal energy at a given temperature can promote electrons between them. Although these benefits exist, optical techniques still depend on the use of sensitive and stable probes (Silva et al., 2017).

Rajashree Panda et al (Panda et al., 2025) also noted that increasing the operating temperature affects the photoluminescence intensity or brightness, phenomenon known as thermal quenching. If the emission peak has a combination of any two thermal quenching mechanisms, it can be harnessed for various applications.

Luminescence-based thermometers have been thoroughly examined and provide accurate measurement of temperature. According to Miroslav D. Dramicanin (Dramićanin, 2020) depending on the application temperature readout strategies can vary. And luminescence thermometry probes can be selected based on the target environment, whether it is biomedical, micro or nanoscale, or high-temperature engineering.

When conducting temperature measurements, several parameters are essential for evaluating performance. These parameters include absolute and relative sensitivities among others. These performance parameters are important because they evaluate the performance of the proposed sensor.

To measure the temperature using luminescence, different types of temperature sensing techniques can be employed such as emission intensity, bandwidth, band position, and spectral shape - specifically the luminescence intensity method LIR. Miroslav D. Dramicanin (Dramićanin, 2020) further explained that luminescence intensity ratio (LIR) is more convenient, straightforward, requires less advanced instrumentation, and is well suited for thermal imaging. This method relies on spectral-shape-based thermometry between two emission bands. Therefore, this study will utilize the LIR method.

1.2 Problem statement

Inorganic crystals doped with rare earths are promising systems for applications based on luminescence, such as optical thermometry. Amongst the myriads of crystalline hosts, garnet-type single crystals such as terbium gallium garnet (TGG), yttrium aluminium garnet (YAG) and terbium aluminium garnet (TAG) exhibit unique properties due to their continuous, uniform, and highly ordered structure which make them suitable hosts for rare earth dopants.

Another promising crystalline system, although less investigated, is the yttrium gallium garnet (YGG). Moreover, by doping this system with different rare earth ions opens a wide range of possible applications, exploiting the luminescence properties of the dopants species. Limited studies have evaluated the spectroscopic behavior and thermometric performance of yttrium ytterbium gallium garnet doped with Tm^{3+}.

Although Tm^{3+} ions exhibit multiple emission bands in both the visible and near-infrared regions, their suitability for optical temperature sensing in YYbGG crystals under both downconversion and upconversion excitation is yet to be investigated.

Therefore, there is a need to study the spectroscopic properties and temperature-dependent luminescence of Tm^{3+}-doped YYbGG crystals in order to assess their potential for optical thermometry applications.

1.3 Aims and objectives

1.3.1 General Objectives.

- To characterize the photoluminescent processes exhibited by Tm:YYbGG crystals.

1.3.2 Specific Objectives.

- To investigate frequency upconversion and downconversion emissions in Tm:YYbGG crystals under infrared excitation.
- To evaluate the suitability of the crystals as luminescent probes for optical thermometry.

2. Literature Review

2.1 Rare Earth Elements

The rare earth (RE) elements are a group of 17 closely related elements, commonly known as lanthanide ions, as shown in the periodic table 2.1 (Voncken, 2016).

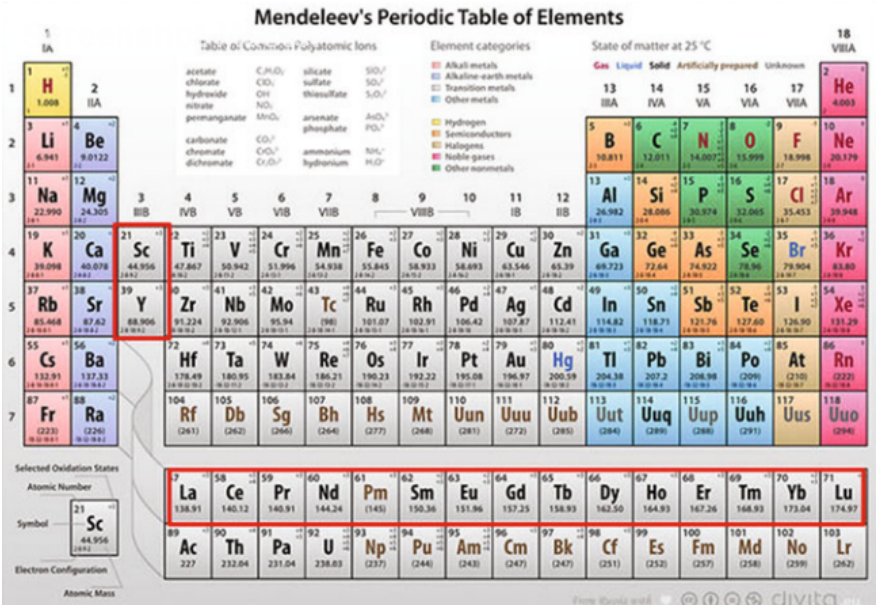

Figure 2.1: The Periodic System of the Elements (Voncken, 2016),The REE including Sc and Y, are outlined in red

The main difference of these atoms, compared to other elements, is that as the atomic number increases, the inner $4f$ shell is filled rather than the outer shells. Their ions are widely used in applications such as lasers, phosphors, fibers, and amplifiers. This due to their narrow emission, long luminescence lifetime, and a unique configuration of electron energy levels (Marciniak et al., 2022).

Rare earth elements also known as lanthanides (Ln^{3+}) are often found in crystals as divalent or trivalent cations. Divalent ions have an outer electronic configuration of $4f^{(n-1)}5d$, where n represents one more electron compared to trivalent ions. This corresponds to the electronic configuration $4f^n$. Optical transitions occur in this configuration and are characterized by parity-allowed transitions, broad absorption and emission bands.

In contrast, trivalent lanthanide ions possess a $4f^n$ outer configuration responsible for optical transitions (Solé et al., 2005; Voncken, 2016). The light emitted by these materials is associated with $4f - 4f$ electronic relaxations of the Ln^{3+}. This luminescence is not parity allowed and the emission is weak compared to divalent lanthanides. Despite this, trivalent ions are mostly used in experiments due to their stability, narrow emission band, wide spectral range, and long lifetimes (Laia et al., 2020).

2.1.1 Lanthanide Energy Levels.

Lanthanide (Ln^{3+}) energy levels can be determined and described within the framework of atomic theory formalism, where the electrostatic Hamiltonian that describes a Ln^{3+} ion composed of N electrons and a nucleus of charge Ze is given by:

$$H_{\text{electrostatic}} = H_0 + H_{re} + H_{so} + H_{\text{terms}} \tag{2.1.1}$$

where H_0 represents the kinetic energy and the potential interaction between the N electrons and the field created by the nucleus, H_{re} is the Coulomb interaction between pairs of electrons, H_{so} is the spin-orbit interaction, and H_{terms} corresponds to other weaker electrostatic and magnetic interactions such as spin-spin and spin-other-orbit couplings.

The non-relativistic part of the Hamiltonian of a free ion with N electrons and a point nucleus of unlimited mass can be expressed as:

$$H_{\text{electrostatic}} = H_0 + H_{re} = \sum_{i=1}^{N} \left[-\frac{\hbar^2}{2m}\nabla_i^2 - \frac{Ze^2}{r_i} \right] + \sum_{i>j} \frac{e^2}{r_{ij}} \tag{2.1.2}$$

where $\hbar$, e, m, and r_{ij} are the Planck constant, electron charge, electron mass, and the inter-electronic distance, respectively.

The central field approximation is applied because the $4f$ electrons are the most important from the optical spectroscopy viewpoint. This approximation assumes that the $4f$ electrons move independently within a total field, which is the sum of the field produced by the ion's nucleus and the symmetrical field created by the electrons in the filled shells, together with the remaining $4f$ electrons.

Under this approximation, Eq (2.1.2) can be rewritten as:

$$H_{\text{electrostatic}} = H_0' + H_{re}' = \sum_{i=1}^{N} \left[-\frac{\hbar^2}{2m}\nabla_i^2 - V(r_i) \right] + \sum_{i>j} \frac{e^2}{r_{ij}} \tag{2.1.3}$$

where this new Hamiltonian only accounts for the contribution of the $4f$ electrons to the energy (Rodríguez, 2018).

P.S. Peijzel (Peijzel et al., 2005) reported that numerous measurements of energy levels of the $4f^n$ configurations of lanthanide ions in several host lattices were conducted in the 1950s and 1960s by Dieke. These measurements were arranged in what is referred to as a Dieke diagram. The diagram enables identification of the energy levels in new host materials and has been an essential tool in designing materials suitable for phosphors or lasers.

Dieke's experimental spectral measurements were performed using systems composed of rare earth ions placed in the lanthanide chloride ($LaCl_3$) host, as illustrated in Figure 2.2. Excitation to any of the energy levels above the ground state can result in emission, with the outcome depending on the phonon spectrum of the host matrix (Dejneka et al., 2003; Oyebola et al., 2015).

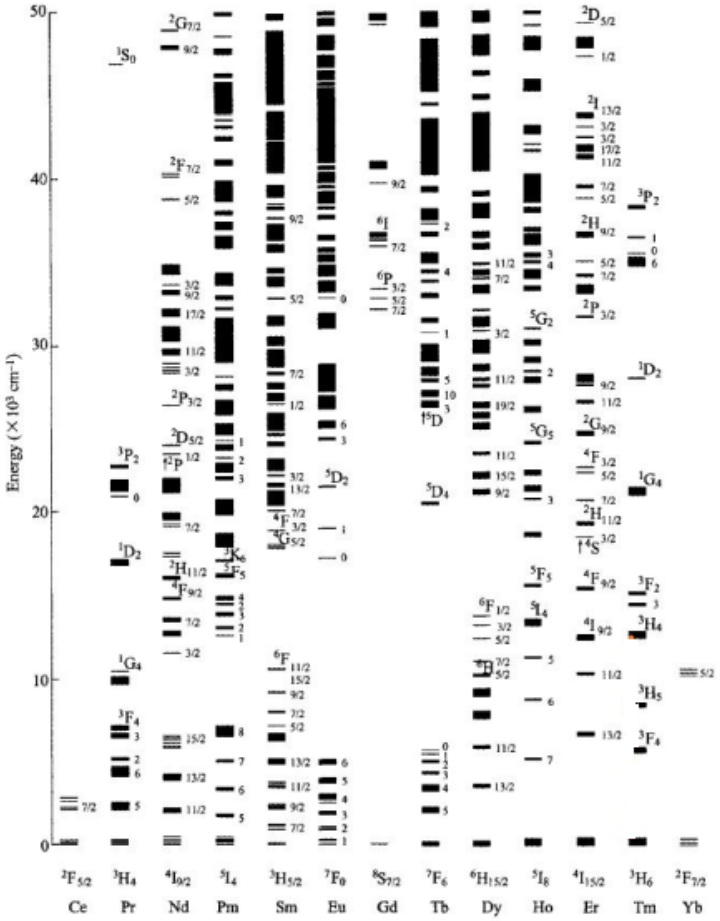

Figure 2.2: An energy level diagram of trivalent rare earth ions in LaCl_3 (Oyebola et al., 2015)

In the case of spectroscopy, the electrons occupying the incomplete $4f$ shell are distributed according to the Pauli exclusion principle. This results in unpaired electrons, which can interact with UV, visible, or IR radiation. Unlike transition metals, the $4f$ electrons of the lanthanides do not form bonds with the surrounding environment, as they are firmly shielded by the $5d$ and $6s$ electrons. (Rodríguez, 2018).

2.1.2 Crystal field interaction: Ln^{3+} ion in a host matrix.

When a Ln^{3+} ion is introduced into a solid matrix, the influence of the host material on the ion is seen through the weak electric field interaction with the $4f$ electrons. This interaction leads to an increase in the degeneracy of the free-ion energy levels, which in turn causes the splitting of the energy levels.

The crystal field responsible for this splitting contains the same point symmetry as the Ln^{3+} ion site. Hence, the observed absorption and emission spectra of the ion are directly related to this symmetry. In other words, the fine-structure levels and the intensities of radiative transitions

between levels of the same ion may differ depending on the host material.

The Hamiltonian that describes the influence of the host matrix ligands on an optically active Ln^{3+} ion can be written as:

$$H_{\text{ion+matrix}} = H_{\text{free ion}} + H_{\text{electron-static matrix}} + H_{\text{electron-dynamical matrix}} + H_{\text{dynamical matrix}}. \quad (2.1.4)$$

a) $H_{\text{free ion}}$: Hamiltonian that describes the isolated ion.

b) $H_{\text{electron-static matrix}}$: describes the host matrix effect on the Ln^{3+} ion. It is also known as the *static crystal field interaction*.

c) $H_{\text{electron-dynamical matrix}}$: describes the effect of the vibrational modes of the host ions on the Ln^{3+} ion, through $4f$ electron-phonon coupling.

d) $H_{\text{dynamical matrix}}$: represents the vibrational energy of the host matrix atoms, which is responsible for the non-radiative de-excitation between Ln^{3+} ion levels.

Since the last two interactions are weaker than the static crystal field, perturbation theory can be applied to the Ln^{3+} ion levels. These interactions play a key role in optical transitions between the levels, changing the shape and intensity of electronic transitions, giving rise to vibronic bands, or producing non-radiative processes. (Rodríguez, 2018).

2.1.3 Applications of Rare Earth Elements.

1 Biological Applications

Lanthanide luminescence can be applied in biological analysis because, the absorption of biological matter, water and hemoglobin, is weak in the biological windows(I-BW, II-BW, III-BW). This reduces absorption and luminescence from other biological samples, such as proteins and nucleic acids. The NIR excitation also reduces photo-damage and allows deep penetration, enhancing the signal-to-noise ratio and detection. Additionally, the intracellular concentration of an analyte can be determined with very long luminescence lifetimes through time-gated measurements (Chatterjee et al., 2008; Mader et al., 2010).

2 Cancer Therapy

Lanthanide upconverting nanoparticles have been applied in cancer photodynamic therapy. The nanoparticles are injected into the bloodstream and remain in normal cells for several hours, but carry on in cancer cells for a longer period of time. After some time, a 980 nm excitation source irradiates the affected area, activating the photosensitizer in cancer cells, which releases active singlet oxygen ($^1O_2$) that can potentially kill the cancer cells (Qian et al., 2009; Wang et al., 2013a).

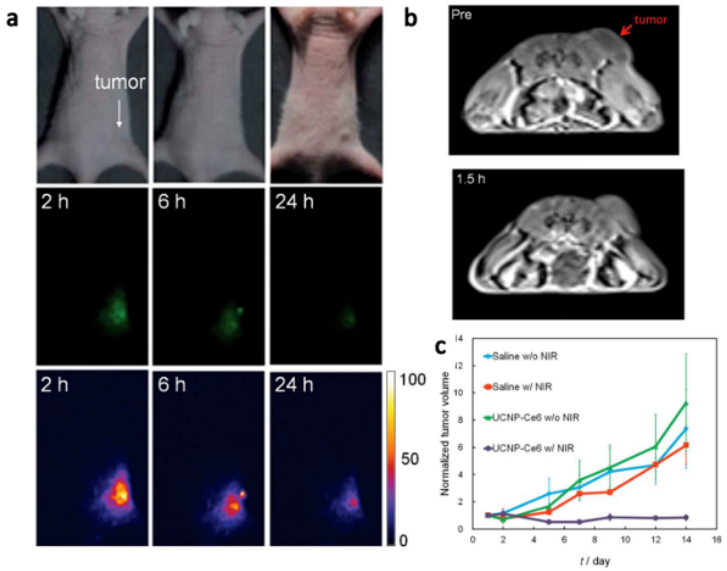

Figure 2.3: In vivo imaging-guided Photo dynamic therapy, (a) UCL images of nude mice bearing tumors after injection of UCNP, (b) MIR images of a tumor-bearing nude mouse before and after 1.5 h injection of UCNP, (c) Growth of tumors after various treatments indicated for efficient imaging guided Photo dynamic therapy (Wang et al., 2013a).

3 Temperature Sensors

Temperature is a critical parameter affecting living cells. Thermal sensing must therefore be achieved with minimal changes to the surrounding environment. Luminescent micro or nano-particles can be used for temperature sensing by analyzing either spectral intensities or bandshape changes between energy levels (Hoyt and Sheik-Bahae, 2000).

4 Efficient Solar Cells

Lanthanide-based nanoparticles show great potential in the improvement of solar cells by enhancing the efficiency of the P3HT organic solar cells. In conventional solar cells, photons with energy below the cell's bandgap are lost. However, through upconversion the low energy photons can be converted into higher energy photons which can be utilized by a solar cell (Méndez et al., 2010).

5 Security Printing Inks

Won Jin Kim (Kim et al., 2009) reported the use of Er:Yb:NaYF_4 and Tm:Yb:NaYF_4 nanoparticles in security printing inks, applied in the printing of invisible quick-response (QR) codes on paper. When illuminated by NIR light, the QR code becomes visible and can be read by a smartphone. These nanoparticles are chemically and mechanically stable, and remain undamaged from the stresses of being applied to paper. This technology can be extended to printing on glass and flexible plastic films (Chai et al., 2010).

6 Lighting Devices

Lanthanide upconverting particles are attracting attention for applications as visible and NIR-emitting phosphors. Upon excitation of the Yb^{3+} as a sensitizer co doped with other

lanthanides elements such as erbium and thulium. These emit green, red and blue luminescence respectively. The emissions can be combined to obtain white light. This technology can be applied in liquid crystal displays as back up lighting. The current white-light sources have broad emission spectra requiring most generated light to be filtered (Albino et al., 2024; Biao et al., 2008).

Rare earth elements such as ytterbium, erbium, yttrium, neodymium, and thulium have been thoroughly explored as dopants in silicon fibers, glass, phosphors and lasers. However, this study will specifically focus on thulium and ytterbium due to their broad bandwidth, efficient upconversion and downconversion properties, and growing importance in NIR-infrared laser applications.

2.1.4 Thulium (Tm).

Thulium (Tm^{3+}) is a rare earth element well known, for its high chemical stability, excellent insulating properties as well as interesting dielectric characteristics (Zdanowlcz, 1988). It is the thirteenth lanthanide element and has 12 electrons in its $4f$ shell.

Energy Levels of Thulium

Energy levels of thulium that are relevant to this study,

1. $^3H_6$

   This is the ground state energy level of Tm^{3+}.

2. $^3F_4$

   This is the first excited state of Tm^{3+} and is located at $\sim 6000\,\text{cm}^{-1}$ above the ground state. The $^3F_4 \rightarrow {}^3H_6$ transition produces a wide emission band spanning $1.6 - 2.0\,\mu$m. The large linewidth of the emission suggests a strong coupling of the rare-earth ion to the lattice (Tropper et al., 1991). The $^3F_4$ energy level can be pumped directly at around 1650 nm, or indirectly through the decay of higher-energy states such as $^3H_5$, $^3H_4$ and $^1G_4$ (Jackson and Mossman, 2003; Tropper et al., 1991).

3. $^3H_5$

   The $^3H_5$ energy level is located at approximately $8000\,\text{cm}^{-1}$ above the ground state and $2250\,\text{cm}^{-1}$ above the $^3F_4$ energy levels. Due to the small energy gap between the $^3H_5$ and $^3F_4$ energy levels, nearly all of the excited ions in the $^3H_5$ energy level decay non-radiatively to the $^3F_4$ energy level. The dominance of this non-radiative decay suppresses the possibility of observing radiative emission from the $^3H_5$ energy level (Digonnet, 2001).

4. $^3H_4$

   The $^3H_4$ energy level is the third excited state of Tm^{3+} and is located at approximately $12{,}300\,\text{cm}^{-1}$. Relaxation to the next lower energy state, the $^3H_5$ energy level, can occur either radiatively or non-radiatively, depending on the host material (Miniscalco, 2001). A second possible radiative transition, $^3H_4 \rightarrow {}^3H_6$, is the dominant radiative relaxation

path from the $^3H_4$ energy level. The radiative transitions from the $^3H_4$ energy level namely $^3H_4 \rightarrow {}^3F_4$ and $^3H_4 \rightarrow {}^3H_6$ produce emission bands ranging 1460–$1530,$ nm and 770–$820,$ nm, respectively. Among these, the $^3H_4 \rightarrow {}^3F_4$ transition has attracted significant attention in recent years due to its potential for optical amplification in the telecommunications S-band (Smart et al., 1990, 1991).

5. $^3F_{2,3}$

The $^3F_2$ and $^3F_3$ energy levels are located at approximately 15,100 and 14,550 cm^{-1} above the ground state, respectively, and are separated by approximately 550 cm^{-1}. This small separation allows them to be thermally coupled, meaning their population is governed by the Boltzmann distribution. Thermalized energy levels in lanthanide materials have been extensively used in temperature measurements. However, the close spacing between $^3F_2$, $^3F_3$, and the lower $^3H_4$ energy level leads to efficient non-radiative relaxation, thereby suppressing any radiative emission from the $^3F_2$ and $^3F_3$ energy levels (Wade et al., 2003). These two energy levels can be directly pumped with 660 nm and can be used to excite the $^1D_2$ energy level through an Excited State Absorption (Walsh and Barnes, 2004).

6. $^1G_4$

The $^1G_4$ energy level of Tm^{3+} is located at approximately 20,600 cm^{-1} above the ground state. Radiative emission from the $^1G_4$ level can occur through several transitions such as the $^1G_4 \rightarrow {}^3F_4$ (650 nm) blue, and $^1G_4 \rightarrow {}^3H_6$ (480 nm) red emissions (Walsh and Barnes, 2004)

7. $^1D_2$

The $^1D_2$ energy level of Tm^{3+} is located at approximately 28,000 cm^{-1} above the ground state. In the three-photon absorption upconversion processes these transitions $^1D_2 \rightarrow {}^3H_5$ (522 nm and 543 nm), $^1D_2 \rightarrow {}^3F_4$ (452 nm), and $^1D_2 \rightarrow {}^3H_6$ (363 nm), were observed from thulium doped samples (Li et al., 2009; Tian and Reddy, 2001)

Applications of Thulium

Thulium doped fibers have many applications including spectroscopy, remote sensing, photomedicine, material processing, mid-IR generation in high-power lasers (Agger and Povlsen, 2006; Li et al., 2013). When doped into silica fibers, thulium provides enhanced amplification bandwidth of about $30THz$, which is significantly broader than that of erbium. Additionally, Hoyt and Sheik-Bahae (Hoyt and Sheik-Bahae, 2000) explained how thulium-doped glass was used in the observation of anti-Stokes fluorescence cooling.

Furthermore, thulium doped fiber lasers have an absorption coefficient in water-containing tissue that is four times higher than that of Holmium:YAG and they can operate with smaller fiber sizes. This makes them advantageous for laser technology applications, particularly in the field of urology (Rice and Somani, 2021).

2.1.5 Ytterbium(Yb).

Ytterbium is the fourteenth lanthanide element and has 13 electrons in its 4f shell and has two valence states $+2$ and $+3$. The ytterbium ion has the simplest energy level structure of all the rare earth ions, with an excited state of approximately 10 000 cm^{-1} from the ground state (Simpson, 2020). Ytterbium only has two energy levels $^2F_{7/2}$ and $^2F_{5/2}$, this reduces the possibility of excited state absorption, however, it can be used as both an emitter or/and sensitizer. Additionally ytterbium exhibits a broad absorption and emission spectra under 980 nm excitation (Jha, 2014).

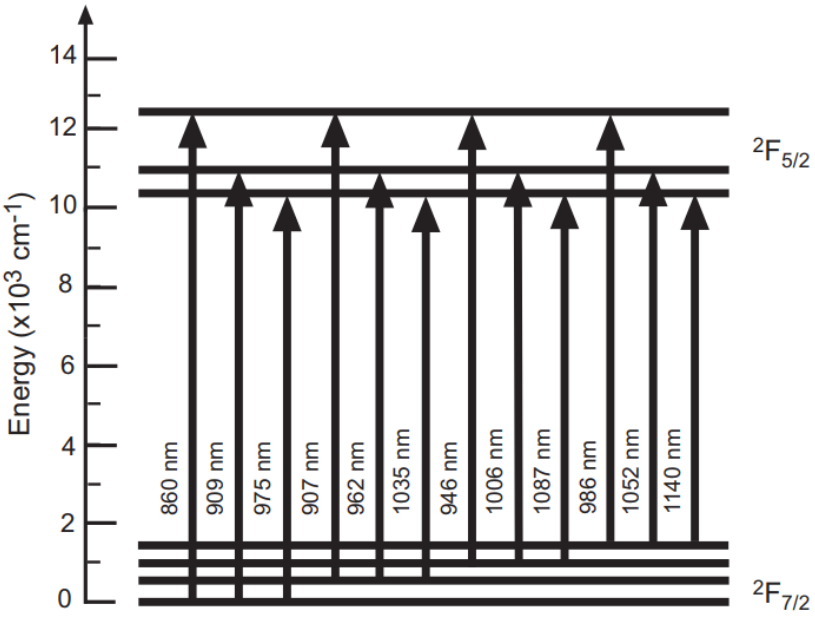

Figure 2.4: Energy level diagram of Yb^{3+} (Simpson, 2020)

Applications of Ytterbium

Ytterbium oxides can be found in several forms such as nano powders and pellets. These are used for optical coating and thin films applications. This rare earth material has a stable and nonradioactive isotope that is mostly used in medical research, this isotope can be used in acquiring important physical and chemical analytical techniques and properties, such as x-ray diffraction, surface area analysis, and other critical parameters of certain industrial materials. Ytterbium based lasers offer excellent beam quality and low noise levels and Yb-based fiber-optic amplifiers yield excellent overall performance over wide spectral regions (Jha, 2014).

2.2 Optical or Luminescence Spectroscopy

Spectroscopy is a study that focuses on the interaction of matter with radiation. This includes; absorption, reflection, emission, and scattering. There are different branches of spectroscopy, however in this study we shall focus on optical spectroscopy. This is the interaction of matter with ultra violet, visible or, infrared radiation within the optical range (Solé et al., 2005). When an

electron is excited with either infrared or visible radiation, a photon is absorbed and the electron is rapidly promoted to an excited state, where the electron maintains the same spin as in its ground state. Relaxation back to the ground state can occur through either non-radiative or radiative processes, depending on the local environment of the electron. In radiative processes the relaxation is accompanied by the emission of a photon (Richards-Kortum and Sevick-Muraca, 1996).

2.2.1 Radiative emission.

Radiative emission is a process in which an emitter specie, such as lanthanide ion (Ln^{3+}), for instance, releases photons as it returns to the ground state. During this process there is a probability unique to each electronic level. This probability is denoted by W_{RAD} and it is the inverse of the time taken by the Ln^{3+} ion to return to its ground state. If only the spontaneous emission is considered as the possible de-excitation:

$$\tau_{\text{RAD}} = \frac{1}{W_{\text{RAD}}} \tag{2.2.1}$$

Considering other probabilities such as multiphonon and energy transfer, the experimental time becomes:

$$\frac{1}{\tau_{\text{EXP}}} = W_{\text{RAD}} + W_{\text{MP}} + W_{\text{ET}} = \frac{1}{\tau_{\text{RAD}}} + W_{\text{MP}} + W_{\text{ET}} \tag{2.2.2}$$

where W_{MP} and W_{ET} are the multiphonon and energy transfer processes probabilities respectively (Richards-Kortum and Sevick-Muraca, 1996; Rodríguez, 2018).

2.2.2 Non radiative emission.

Several researchers observed through multiple experiments that the fluorescence in many host materials could only be observed for energy separations greater than $1000\,cm^{-1}$. This led to the discovery of a competing process known as non-radiative decay. Non-radiative transitions involve the absorption and emission of phonons, quanta of vibrational energy in the host material. When electronic states are close enough to be bridged by emission or absorption of one or two phonons, non-radiative decay will occur rapidly. This phenomenon is responsible for the thermalisation of energy levels (Simpson, 2020).

2.2.3 Luminescence mechanisms.

Photoluminescence processes can be divided into downconversion and upconversion. Upconversion also known as anti-stokes luminescence is a non linear optical process that can convert two or more low energy photons (near infrared photons) into one high energy photon and emit it in the visible or ultra violet. In this process light absorption is mediated through energy transfer mechanisms such as ground state absorption, excited state absorption, and energy transfer

upconversion (Albino et al., 2024; Chen et al., 2007).

Downconversion, however, follows the stokes law. In this process a high energy photon is absorbed and converted into a low energy photon. It can be divided into two downshift and quantum clipping. In downshift a high energy photon is absorbed and converted into only one low energy photon, whereas, in quantum clipping, a high energy photon is absorbed and converted into multiple low energy photons. Energy transfer and crossrelaxation can be observed during downconversion (Chen et al., 2023).

Energy Tranfer

Energy transfer occurs when absorption and emission do not take place within the same optically active ion center. Liua and Qiu (Liua and Qiu, 2015) observed that both radiative and non-radiative energy transfer (ET) can be regarded as optical processes because they involve electromagnetic transfer, only radiative energy transfer is mediated by a photon, while non-radiative processes involve energy transfer without the emission of light, such as multi-phonon emission. Multi-phonon relaxation processes convert the electronic excitation partially or completely into vibrational energy (phonons) (Solé et al., 2005).

Optical Energy transfer can take place via resonance between spatially separated donor and acceptor pairs within solids. Additionally, energy transfer can be used to modulate emission spectra and to generate upconversion and down conversion emissions in many rare-earth doped systems. Such Energy tranfer processes include excited-state absorption (ESA), ground-state absorption (GSA), cross relaxation (CR) ,energy transfer Upconversion (ETU) among others (Chen et al., 2025).

1 Cross relaxation

Cross relaxation is an energy transfer process that takes place through dipole - dipole interactions, which is a type of ion-ion energy transfer that depends on the distance between a donor and an acceptor. It can also occur using a single type of lanthanide ion that plays the role of both donor and acceptor (Peng et al., 2021).

During this process as the donor ion relaxes it transfers part or all of its energy to a nearby acceptor ion. The energy gap between the donor and acceptor must be equally spaced, in this case the energy transfer is said to be resonant. If there is an energy mismatch, it can be compensated for by the absorption and emission of phonons, this is known as phonon assisted energy transfer (Simpson, 2020). An example of a well known cross relaxation process in Tm^{3+} is presented in figure 2.5.

In this process, if an ion is excited to the $^3H_4$ energy level interacts with a nearby ion in the ground state $^3H_6$, the excited ion can transfer part of its energy to the ground state ion, leaving them both in the $^3F_4$ intermediate state.

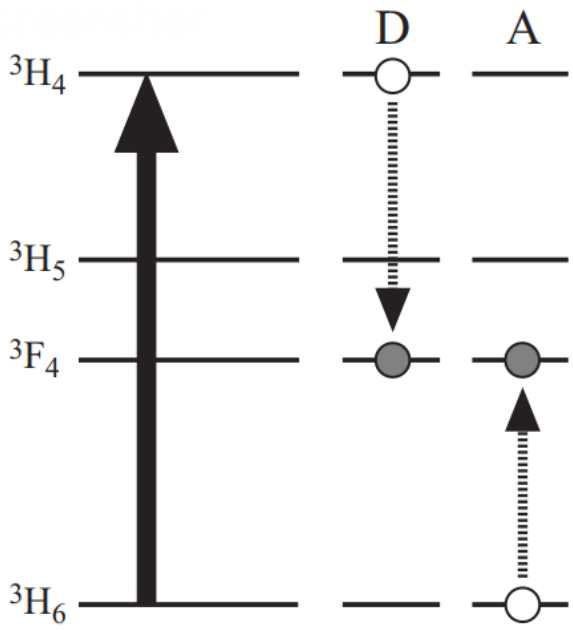

Figure 2.5: Cross relaxation process in Tm^{3+} between the $^3H_4$ and $^3H_6$ energy level. The donor ion is labeled D and the acceptor ion is labeled A (Simpson, 2020)

2 Excited state absorption and Ground state absorption

Excited state absorption and ground state absorption involve photon absorption by an ion, leading to excitation to a higher energy state. In ground state absorption , the ion is initially in the ground state when it absorbs the photon, while in excited state absorption, the ion is already in an excited state and absorbs an additional photon to reach a higher excited level (Chen et al., 2025).

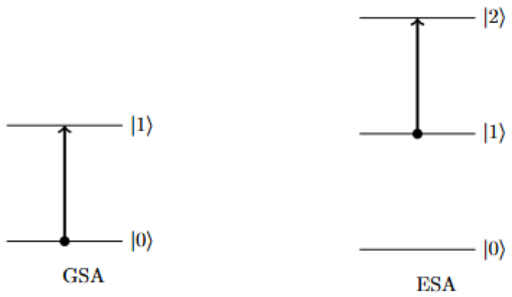

Figure 2.6: Excited state absorption (ESA) and Ground state absorption (GSA) (François et al., 2000)

3 Energy Transfer Upconversion (ETU)

Energy transfer upconversion (ETU) involves both donor and acceptor ions being in excited states. In this process, as the donor ion relaxes as it transfers part or all of its energy to a nearby acceptor ion. the acceptor ion will therefore elevate to a higher energy state. From this state, the acceptor can relax either radiatively or nonradiatively to lower levels, or radiatively directly to the ground state (Simpson, 2020).

Excited-state absorption and energy transfer upconversion are quite similar processes because the ion is not initially in the ground state, however, in excited-state absorption, the same ion sequentially absorbs multiple photons, which makes it concentration dependent. Whereas, in energy transfer upconversion a pair of interacting ions occurs, making the process both concentration and pump power dependent (Gebavi et al., 2010; Liua and Qiu, 2015). The figure below shows an example of Energy transfer upconversion in Tm^{3+}.

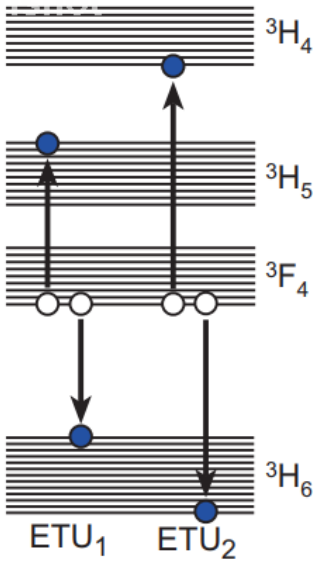

Figure 2.7: Energy transfer up-conversion process from the $^3F_4$ energy level in a Tm^{3+} doped sample (Simpson, 2020)

Figure 2.7 shows the two possible energy transfer up-conversion processes that quench the population of the $^3F_4$ energy level (Simpson, 2020). Building on this understanding of energy transfer mechanisms, this study investigates the non-radiative and radiative energy transfers taking place in yttrium ytterbium gallium garnet doped with thulium.

2.3 Luminescence thermometry

Temperature is an important thermodynamic parameter, essential in both scientific and practical applications. It is used in the diagnosis of medical conditions, as increased temperature is one of the symptoms of inflammation and disease. Additionally, in industry, temperature regulates the pace and nature of production processes, and its control enables equipment diagnostics. Because accurate measurement of temperature is crucial in both medicine and industry, sensitive and reliable sensing techniques are required (Dramićanin, 2020). Conventional thermometers such as liquid-in-glass thermometers, thermocouples, pyrometers, and thermistors—are widely used in medicine and industrial manufacturing. However, with the increasing technological demands in fields like microelectronics, cell biology, microfluidics, and nanomedicine, these traditional methods have become less effective (Kim et al., 2017).

Luminescence thermometry has emerged as a key approach for achieving high spatial resolution and accurate temperature measurements. It represents a new generation of small scale thermometers and serves as a powerful tool for advancing our understanding of micro - and nanoscale electronic devices, and integrated photonic systems, etc (Dramićanin, 2020).

2.3.1 Luminescent thermometers.

Luminescence thermometry exploits the temperature-dependent luminescence of materials such as Ln^{3+} - doped phosphors. In this technique, the temperature is determined by analyzing the luminescence spectrum of the phosphor and how the spectrum behaves with temperature (Marciniak et al., 2022). Due to its sensitivity and versatility, luminescence thermometry also fulfills the key requirements of an ideal thermometer (Geitenbeek, 2018; Jaque and Vetrone, 2012). A wide range of luminescent materials have been employed as luminescent thermometers, these include; semiconducting quantum dots, rare-earth-doped nano or micro crystals, and metal nano or micro clusters, as well as organic systems like polymers, organic dyes, biomolecules (Zhou et al., 2018), and bulk materials doped with rare earth elements such as glasses, crystals and optical fibers have also been exploited for luminescence thermometry (Wu et al., 2025). The usefulness of these materials as thermometers arises from their photoluminescence properties.

Photoluminescence refers to the emission of light from a material resulting from the radiative relaxation of electrons from excited states to lower energy states. Since the properties of these excited states are temperature-dependent, the resulting emissions also vary with temperature. This makes it both feasible and valuable to investigate different types of luminescent materials with temperature-sensitive characteristics for the development of highly sensitive luminescence thermometers (Chen et al., 2018b).

Building on this principle, optical sensors provide a powerful means of detecting physical or chemical fluctuations in the environment through changes in their optical properties. Among the materials suitable for optical temperature sensing, those doped with trivalent lanthanides are most promising for developing optically active materials, because of their excellent chemical and photostabilty, good biocompatibility, and unique optical features. In particular, they possess thermally coupled levels (TCL), whose relative population varies with the surrounding temperature and, therefore, directly influences their emission (Hernández-Rodriguez et al., 2017). As a result,

extensive research has been undertaken in the use of Ln^{3+}- doped micro and nano materials as optical temperature sensors, and numerous studies demonstrating their potential can be found in the literature.

2.3.2 Applications of Luminescence Thermometry.

Luminescence thermometry has many applications, such as:

1 Biomedicine

Lanthanide doped nano or micro materials exhibit excellent chemical and photostabilty, biocompatibility and, low toxicity. All of which are crucial for biological applications. In particular, Hernandez-Rodriguez (Hernández-Rodriguez et al., 2017) reported that Tm^{3+}/Yb^{3+}- and Nd^{3+}- based optical sensors have been successfully employed in medical applications such as fluorescence bioimaging, cellular temperature probing, and anticancer or photodynamic therapies.

Luminescent probes not only enable luminescence bioimaging but can also support complementary imaging modalities such as magnetic resonance imaging (MRI) and X-ray computed tomography (CT). Additionally, accurate and noninvasive temperature determination is important for studying cellular heat production. Diseases such as cancer are often associated to high temperature or localized temperature increase. Thus, temperature monitoring in cellular activity is essential for early disease detection (Kuruganti and Qi, 2002).

Carrasco et al., (Carrasco et al., 2015) performed *in vivo* photothermal therapy of cancer tumors using Nd^{3+}-doped LaF_3 nanoparticles. Intratumoral temperature was determined from the fluorescence emitted by the Nd^{3+}- doped LaF_3 nanoparticles during hyperthermia treatment. As can be seen from the figure (a), Two tumors were induced in a mouse. One containing Nd^{3+}-doped LaF_3 nanoparticles and the other injected with of phosphate-buffered saline (PBS). The tumor containing luminescent nanoparticles shows bright fluorescence and elevated temperature. Figure (b) shows the temperature profiles recorded during the treatment at different regions of the mouse.

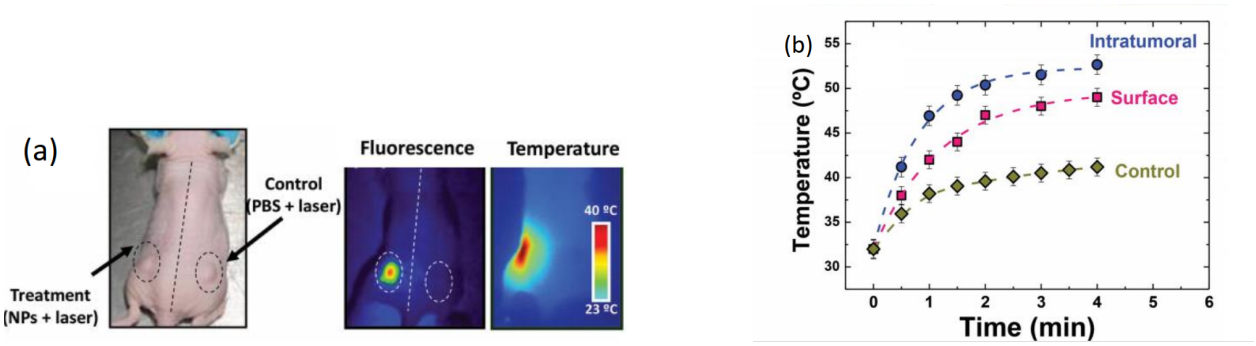

Figure 2.8: Example of lanthanide luminescence thermometry applied *in vivo*: (a) photothermal therapy in a mouse (b) temperature profiles during treatment (Carrasco et al., 2015).

2 Industry

Luminescence thermometry can be used in areas that are inaccessible by other methods because it is a semi-contact technique, making it useful in harsh environments, including high-temperature and cryogenic conditions. As a result, many engineering applications, such as flow temperature measurements and temperature monitoring at engine surfaces, have benefited from this method (Dramićanin, 2020; Hernández-Rodriguez et al., 2017).

According to Geitenbeek (Geitenbeek, 2018) researchers used NaYF_4 doped with Er^{3+} microparticles as tiny thermometers inside a catalytic reactor during the methanol-to-hydrocarbon MTH reaction. By monitoring how the emitted light changed during the reaction, the temperature inside the reactor at different positions was determined. Additionally microparticles can be used to determine the local surface temperature of the heating elements in catalytic systems using the luminescence signal from the crystals.

Recent breakthroughs in luminescence thermometry are emerging across diverse scientific and technological fields (Panda et al., 2025). Building on these advances, the present research focuses on thulium doped in newly synthesized yttrium ytterbium gallium garnet (YYbGG).

2.3.3 Luminescence Thermometry Techniques.

There are several approaches to determining temperature from luminescence, depending on the application and type of luminescence parameter used. Luminescence thermometry can be divided into six different techniques: a) emission intensity, b)emission band shape, c) emission bandwidth d) polarization, e) spectral position, f) lifetime (Dramićanin, 2020; Marciniak et al., 2022) as shown in 2.9.

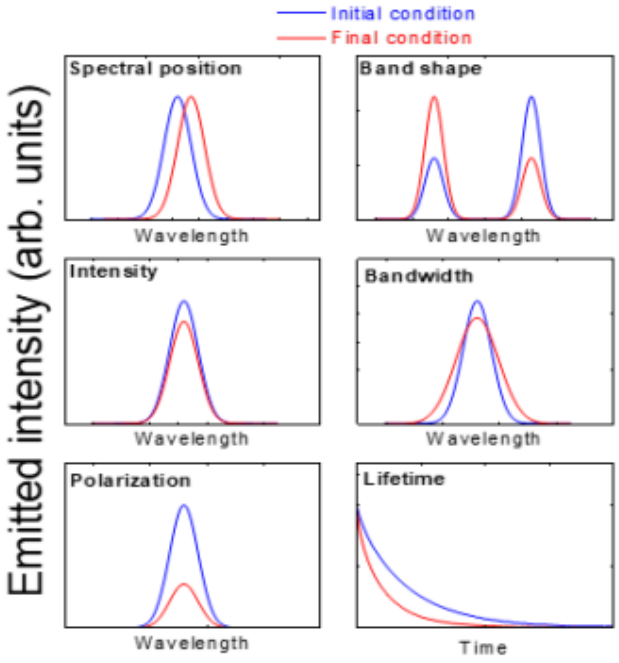

Figure 2.9: Different luminescent responses of an optical sensor due to the the physical or chemical fluctuations of the environment.(Vetrone et al., 2010)

Among these ratiometric methods are the most commonly described, and the choice is mainly according to the working environment (e.g., bio-medical, nano scale, or high-temperature engineering), operating temperature range, precision, and thermometer complexity.

Measurements of the luminescence intensity ratio (LIR) between two emission bands, has emerged as the most widely used approach. This ratiometric method is fast, simple, requires less sophisticated instrumentation, and can be easily adapted for thermal imaging. While temperature can also be determined from absolute changes in luminescence intensity, such measurements are often less reliable due to non-radiative multi-phonon relaxation processes at elevated temperatures. In contrast, LIR relies on the relative population of thermally coupled excited states, which follows the Boltzmann distribution; for this reason, the method is commonly referred to as Boltzmann-type LIR (Dramićanin, 2020; Marciniak et al., 2022; Mi, 2019).

$$LIR = \frac{I_H}{I_L} = B \times \exp\left(\frac{\Delta E}{KT}\right) \tag{2.3.1}$$

where I_H is the intensity of the emission from the higher-energy excited state, I_L is the intensity of the emission from the lower energy excited state, ΔE is the energy difference between the thermalized excited states, and k is the Boltzmann constant $(k = 0.695 cm^{-1}k^{-1})$ and B is the temperature-independent pre-exponential constant. In this case, the relative sensitivity of LIR is a function of temperature, and its value depends only on the energy difference between the thermalized excited states—the larger the difference, the larger the relative sensitivity.

According to Dramicanin (Dramićanin, 2020), evaluating the quality of temperature measurements, parameters such as absolute and relative sensitivities of the measurements must be considered as shown in Table 2.1.

Table 2.1: Mathematical definitions of thermometric parameters (Dramićanin, 2020).

Thermometric Parameter	**Mathematical Definition**
Absolute sensitivity, S_a	$S_a = \frac{d(LIR)}{dT}$
Relative sensitivity, S_r	$S_r = \left\lvert \frac{1}{LIR}\frac{d(LIR)}{dT} \right\rvert \times 100\%$

Luminescence intensity ratio (LIR) was used in this research. Usually the LIR method is used with thermally coupled levels, this is when the distance between the energy levels is about 2000 cm^{-1}. If the distance is more than 2000 cm^{-1}, the levels are considered non thermally coupled. Nevertheless, the LIR between the energy levels can still exhibit a dependence on temperature. This happens because the populations of these levels are interrelated by temperature-dependent transition mechanisms such cross relaxation and phonon-assisted transfers (Laia et al., 2023).

2.4 Optical properties and Application of Yttrium Galium Garnet

The garnet family with general formula $A_3B_2C_3O_{12}$ (A = Ca, La, Tb, Y, Gd or Lu; B = Al, Ga, Fe, Sc; and C = Al, Fe, Ge, or Ga) (Wang et al., 2013b), is an excellent host material due to its high structural stability, low phonon energies, chemical stability, mechanical resistance and specific optical and magnetic characteristics (Albino et al., 2024). Rare-earth-doped materials with a garnet structure have very good properties, these include; high excitation and emission efficiency, uniform distributions of rare-earth ions, a physical and chemical stability, long life, and high thermal conductivity. Owing to these properties, these materials are suitable for use in high-quality white light emitting diode, optical pressure and temperature sensors, laser applications and magneto-optical fields (Zhang et al., 2023).

The Figure 2.10 shows the garnet structure. Three constituents make up the garnet structure, yttrium (cyan), oxygen (red), and a third species that may include Al, Ga, Fe.

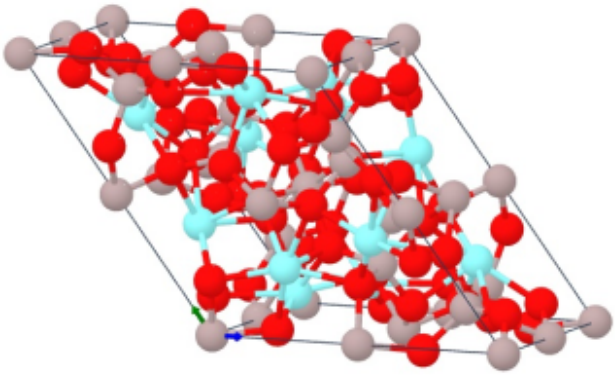

Figure 2.10: Simulated primitive cell of a garnet crystal (Das, 2022)

Yttrium galium garnet ($Y_3Ga_5O_{12}$, YGG) doped with various rare earth ions has been used in many laser and optical sensor applications, including the creation of lasers or wave guides at several frequencies. It has also exhibited potential in creating lenses suitable for high energy lithology (Davidson et al., 2022). Additionally YGG is important in quantum photonics such as quantum information devices. A study by Antariksha Das (Das, 2022) describes how thulium doped yttrium gallium garnet was used to make long-lived and efficient photonic quantum memories, particularly memories for frequency multiplexed quantum repeaters.

Furthermore, an experiment performed by Huiting Zhang (Zhang et al., 2023), revealed that YGG-Sm^{3+} had better results compared to YAG-Sm^{3+}. YGG-Sm^{3+} had a stronger and more intense luminescence peak and color purity useful in white light emitting diodes, this is because Ga^{3+} has a greater atomic mass compared to Al^{3+} which results in the crystal having a higher density and smaller phonon energy. In this study we will focus on yttrium ytterbium gallium garnet doped with thulium.

3. Methodology

3.1 Synthesis and materials

Yttrium ytterbium gallium garnet was synthesized at the laboratório de Vidros Especiais (LaViE), Institute of Chemistry, São Paulo State University (UNESP), Araraquara, SP, Brazil. The following is a brief description of the synthesis of the sample. The analytical grade raw materials used are as follows: PbO (99.99%, Sigma Aldrich), GeO_2 (99.99 %, Sigma Aldrich), Bi_2O_3 (99.99 %, Sigma Aldrich), Ga_2O_3 (99.99 %, Sigma Aldrich), and Y_2O_3 (99.99 %, Lumintech). High purity precursors Yb_2O_3 (99.99 %, Lumintech) and Tm_2O_3 (99.99 %, Lumintech) was used as a dopant for single crystal phases. Additionally HCl (37 %, Exodo Científica) was employed for the extraction of crystals from the glass matrix.

The mixture was placed in a speedmixer equipment for homogenization, after which the stoichiometric parts were weighed. The mixture was then placed on a platinum crucible and put in an electric furnace at 1250° C for 1.5 h. This is the standard procedure for preparing inorganic glasses. After melting the mixture, the furnace was programmed to cool down at a rate of 12° C min^{-1}. This cooling process reduces the viscosity, thereby inducing the formation of the crystalline nuclei and later their growth. After cooling to 900° C , the crucible is removed from the furnace and placed in a highly concentrated Hydrochloride (HCL) bath to dissolve the non crystalline phase and separate the crystals. Upon removing the non crystalline phase, the crystals were washed three times in high purity isopropyl alcohol and then placed in an oven to dry the solvent. This is how YYbGG:Tm^{3+} micro crystals were formed by nucleation and growth into molten glass matrix (Albino et al., 2024).

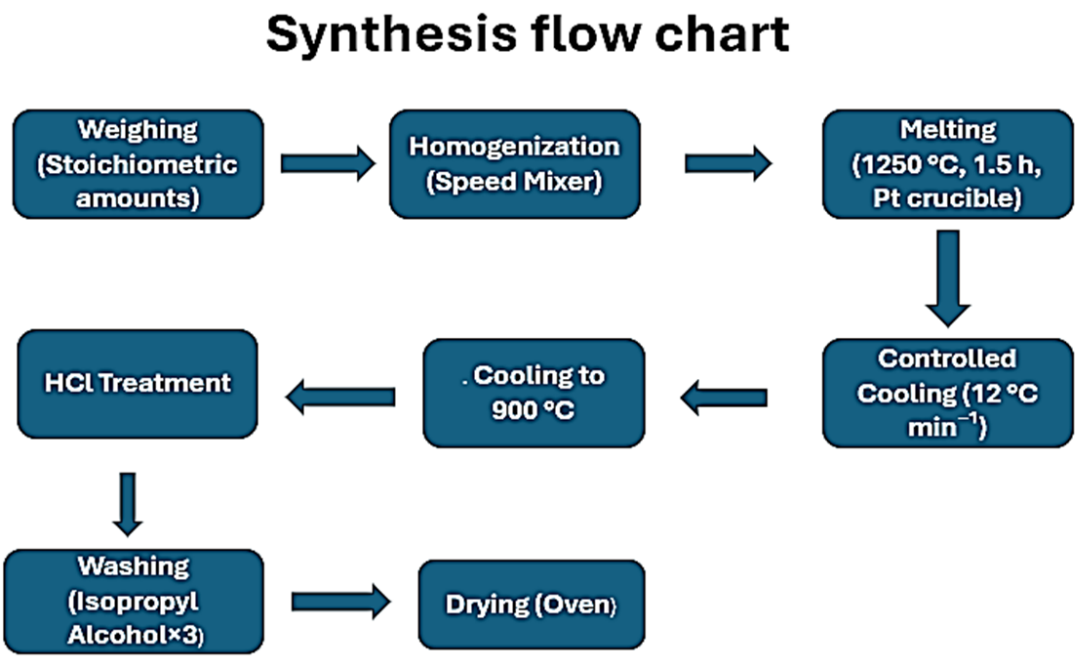

Figure 3.1: Referenced by author

Table 3.1: Composition of the glass used to produce yttrium ytterbium gallium garnet doped with Tm^{3+} crystals (Albino et al., 2024).

Sample	PbO	$Ge0_2$	Bi_2O_3	Ga_2O_3	Y_2O_3	Yb_2O_3	Tm_2O_3
YGG _ YTE	38.0	19.00	23.75	14.25	3.35	1.55	0.10

3.2 Experimental setups and techniques

3.2.1 X-ray diffraction and microscopy.

X-ray diffraction (XRD) powder method was used to confirm the crystaline phase and was carried out using a Rigaku X-ray diffractometer with 40kV/30mA, 0.020° scan step, and a speed of 2° min^{-1}. In the 2θ range from 15° to 90°, at room temperature.

To obtain the optical images, YYbGG - Tm was placed on a rectangular shaped thin film collector and put under the optical microscope model Zeiss Axio lab A1 with lens 50, 100, 200, 500, and, 1000 x having a Axiocam 105 color.

3.2.2 Luminescence.

To obtain the luminescence spectra, the powdered sample was placed into a quartz crucible, which was later placed in a 22 mm diameter silver sample holder in the temperature and environmental control system Linkam FTIR600 shown in figure 3.2. This system allows us to carry out luminescence and spectroscopy analysis of samples from -195°C up to 600°C, with a 0.01 °C of stability.

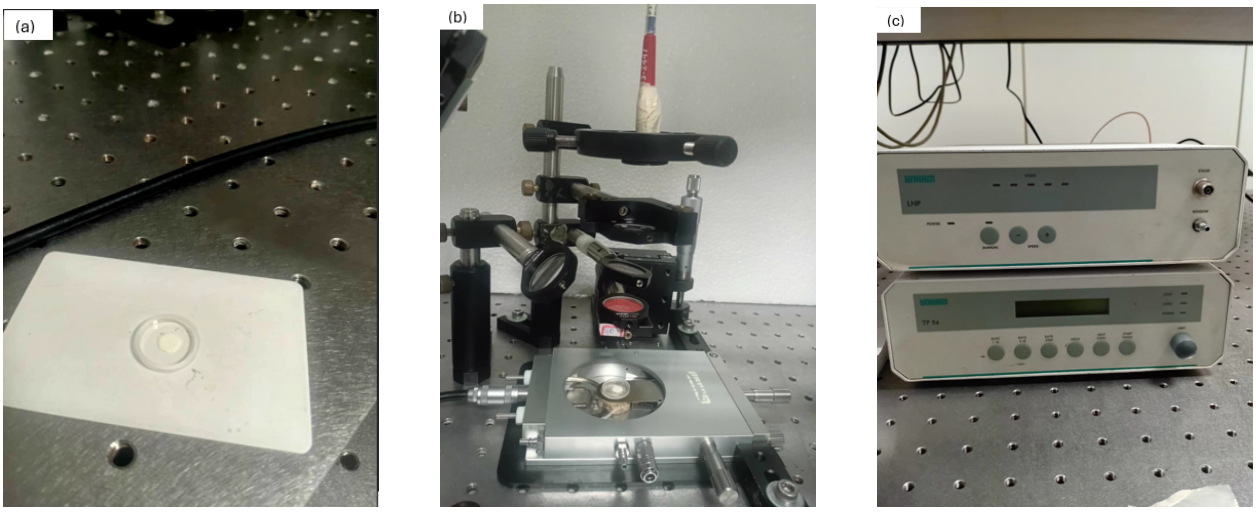

Figure 3.2: Linkam FTIR 600: (a) YYbGG-Tm sample placed on the quarts sample holder (b) linkam FTIR 600 system (c) linkam FTIR 600 system temperature controller

Using this system, spectra measurements were performed varying the excitation power or sample temperature. The sample was excited by two continuous wave lasers, emitting 800 nm and 980 nm. In both cases, visible and infrared luminescence were investigated.

The general experimental setup is presented in figure 3.3. In this setup, the laser beam is directed towards the sample by a set of mirrors. Using a set of half-wavelength plate and polarizer, the excitation power can be adjusted continuously. A 10 cm focal length bi-convex lens is used to focus the laser beam on the sample surface. A lens with a focal length of 5 cm is placed after the sample to collimate the luminescence and a second lens (also with a 5 cm focal length) collects the emission and focuses it on the entrance of the optical fiber. The optical fiber transmits the emission to the spectrometer. Depending on the excitation laser and analyzed emission wavelength range, different set of filters, laser power and spectrometer parameters were employed.

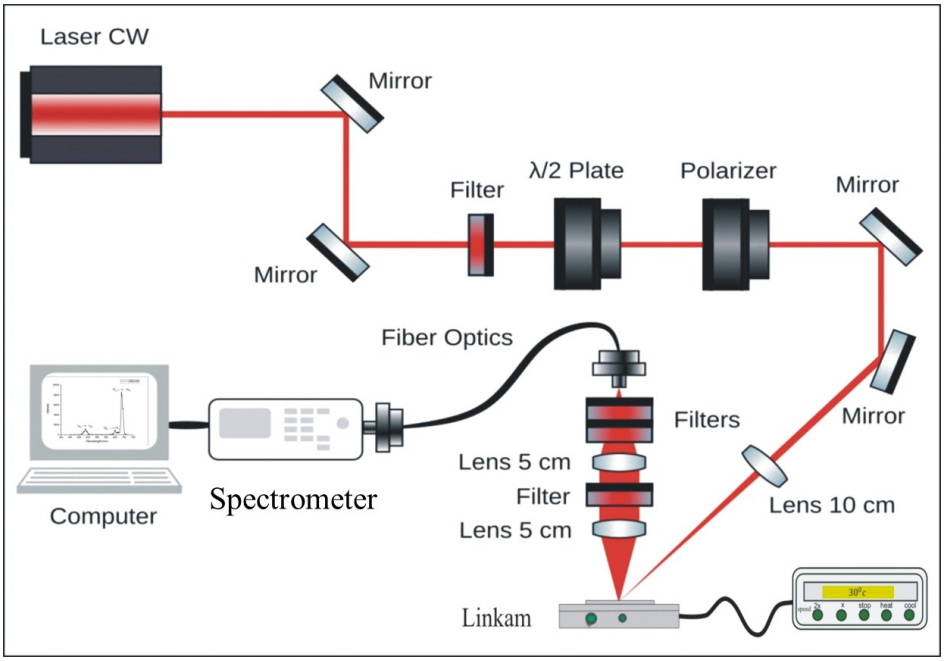

Figure 3.3: Experimental Setup referenced by author

Using 800 nm laser, the temperature-dependent infrared emission was measured fixing the pump power at 30 mW and the sample temperature was varied from 303 to 373 K. The emission was observed using the NIRQuest spectrometer, which detects light in the NIR-infrared range from 900 nm to 1700 nm. A set of optical filters were used an FGL850 filter and an FEL850 filter. The integration time was 3000 ms. The power dependence of the emitted light was performed using the same set up, fixing the sample temperature at 30°C and varying the excitation power from 5 to 50 mW.

For the analysis in the visible range, a pump power of 200 mW was used, and the same temperature range was investigated. Two hot mirrors (0° and 45°) were placed after the sample, and a cold mirror was positioned after the polarizer before the sample; the cold mirror reflects infrared light while the hot mirror reflects visible light. The emission was observed using the 4000USB visible light spectrometer, which detects emissions from 350 nm to 750 nm. During this process the integration time was increased to 25,000 ms in order to collect more light and reduce noise. Using the same setup, the power dependence of the visible emission was analyzed fixing the sample temperature at 30°C, varying the excitation power from 100 to 200 mW.

The same processes was conducted under 980 nm excitation, however a pump power of 60 mW was used within the same temperature range in the visible. In the infrared red, a pump power of 5 mW accompanied with a FEL1100 optical filter was used. The power dependence of both the visible and NIR-infrared range emission was analyzed fixing the sample temperature at 30°C, varying the excitation power from 15 to 60 mW. The integration time in the visible range was 25000 ms and in the NIR-infrared range emission was 350 ms.

4. Results and Discussion

4.1 Properties of Crystal Structure

The optical image of the single crystals produced after the glass matrix separation and cleaning procedure is shown in the figure 4.2. The crystals were observed to have a rhombic dodecahedron and cubic geometry with the sizes being in the range of 15 to 70 μm,

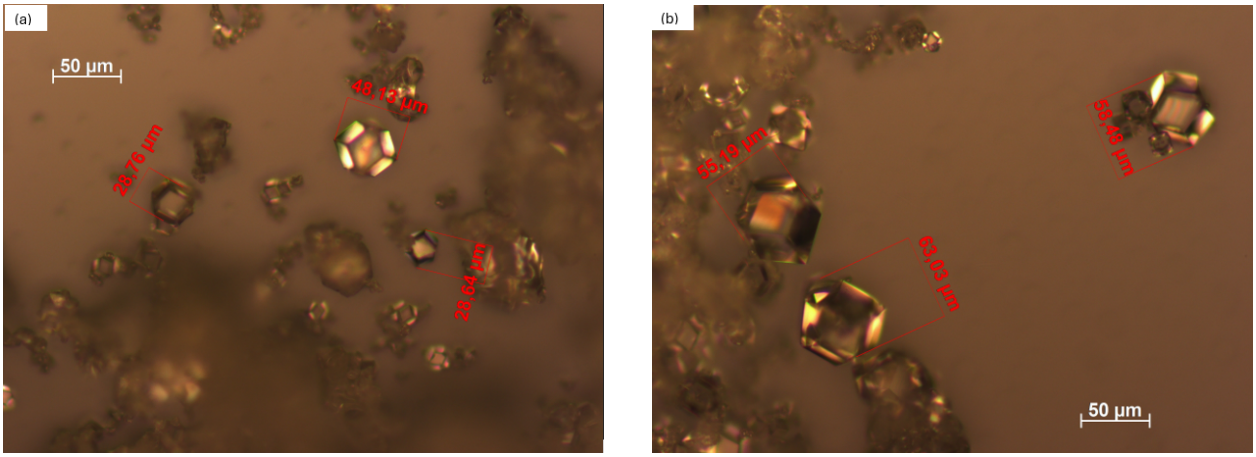

Figure 4.1: Optical microscopy of YYbGG doped with Tm^{3+} crystals, in a $200\times$ objective lens:(a) rhombic dodecahedron, (b) cubic

The results from XRD are in agreement with the results obtained by Leonardo Vieira Albino (Albino et al., 2024) and align with the pattern $Y_3Ga_5O_{12}$ (PDF-ICDD: 73–1373/JCPDS 88–0575), yttrium gallium garnet (YGG) (Nakatsuka et al., 1995).

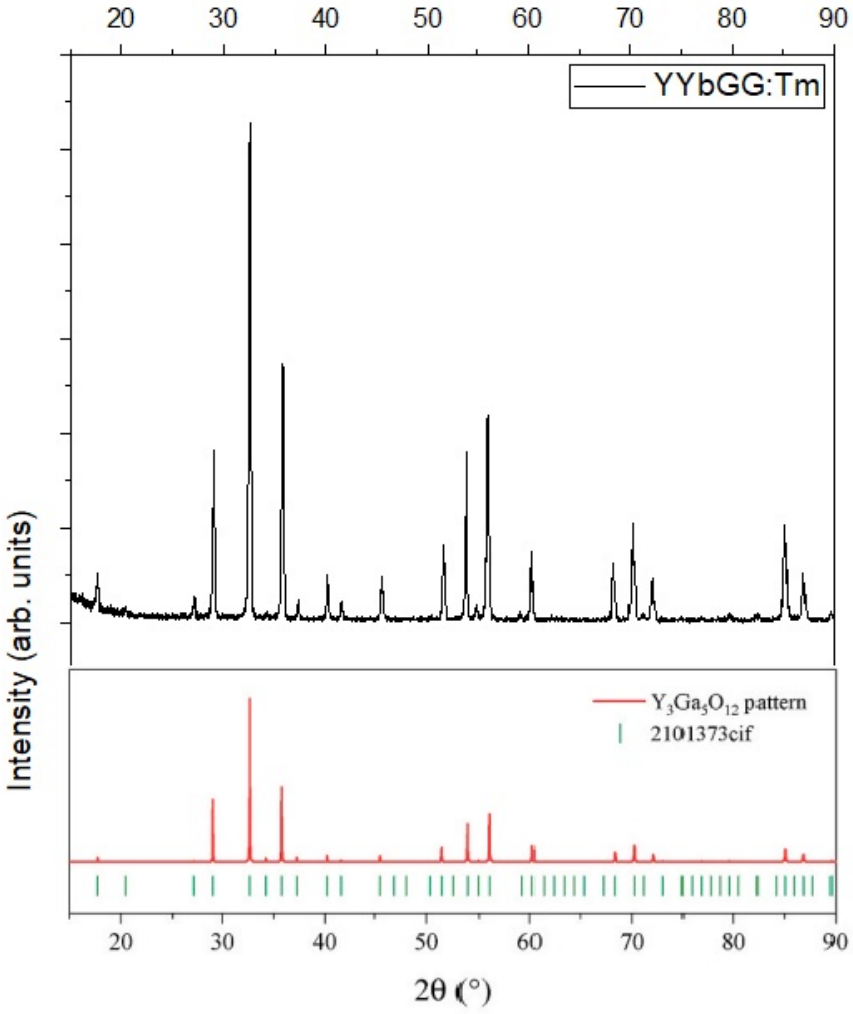

Figure 4.2: XRD results of YYbGG doped with Tm^{3+} crystals

4.2 Luminescence Spectroscopy

The emission can occur through several ways in the YYbGG doped with Tm^{3+} system. This involves different processes such as the ground state absorption (GSA), energy transfer upconversion (ETU), excited state absorption (ESA), and crossrelaxation (CR).

4.2.1 Infrared emission spectra.

Under 800 nm excitation the sample shows emissions at around 1050 nm, 1450 nm and, 1650 nm. Two of the peaks correspond to ${}^3H_4 \rightarrow {}^3F_4$ (1450 nm) and ${}^3F_4 \rightarrow {}^3H_6$ (1650 nm) transitions of Tm^{3+} as shown in the figure 4.3. From the emission spectra it can be seen that 1650 nm emission is more intense than that of 1450 nm emission. The difference in emission intensity is mostly due to the cross relaxation process taking place at $({}^3H_4, {}^3H_6) \rightarrow ({}^3F_4, {}^3F_4)$ and possible energy transfer upconversion at $({}^3F_4, {}^3F_4)$ to $({}^3H_4, {}^3H_6)$.

From figure 4.3, 1050 nm emission peak can be seen, however this emission is not from thulium, but rather from ytterbium. The Yb^{3+} ions are affecting the emission of Tm^{3+}. This is because energy is being transferred from Tm^{3+} to Yb^{3+}. When the sample is excited with 800 nm, the Tm^{3+} ions absorb energy from the ground state ${}^3H_6$ (GSA) to ${}^3H_4$ as the Tm^{3+} ion relaxes energy is transferred to Yb^{3+} ions at ${}^2F_{7/2}$ and excited to ${}^2F_{5/2}$ which later relaxes and emits 1050 nm (Fartas et al., 2020).

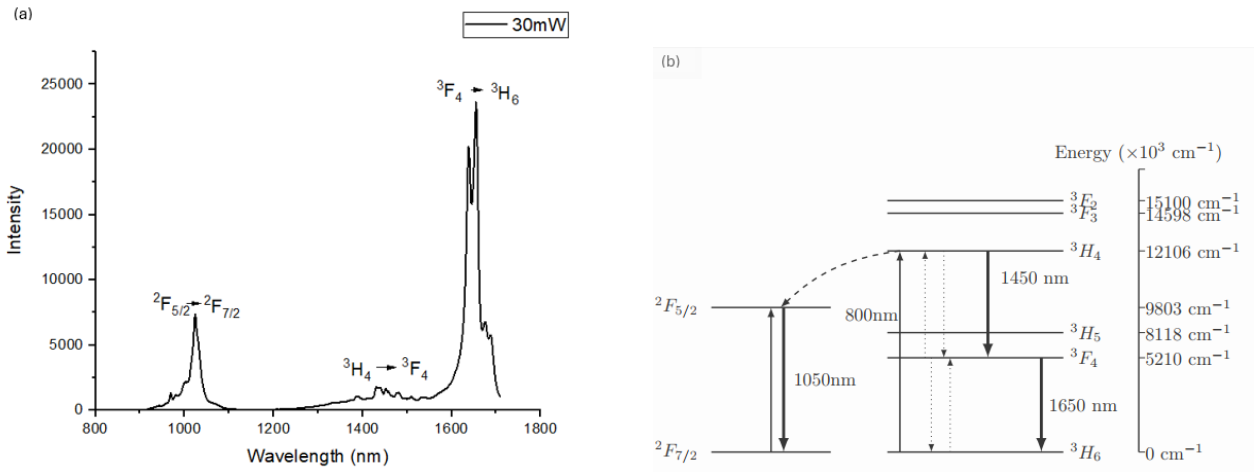

Figure 4.3: Down conversion under 800 nm excitation: emission spectrum (left) and energy level diagram (right)

To verify whether Yb^{3+} affects the emission of the Tm-doped sample, a 980 nm laser was used. Yb^{3+} has a high absorption rate when pumped with the 980 nm laser which explains why the emission spectra under 980 nm is stronger than that of 800 nm. From figure 4.4 the same emission peaks obtained under 800 nm excitation are observed and a weak shoulder can be seen at almost 1100 nm.

Under 980 nm excitation, Yb^{3+} ions absorb a photon from ${}^2F_{7/2}$ and the excited photon rises to ${}^2F_{5/2}$ it later de-excites back to the ground state. As this happens, energy transfer is observed from Yb^{3+} to Tm^{3+}. The energy gap between the different ions does not perfectly match, hence

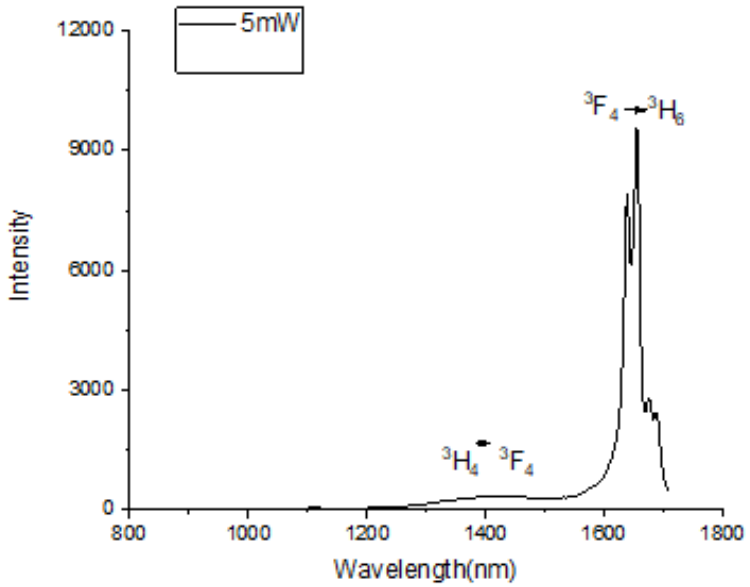

Figure 4.4: Emission spectrum of down conversion under 980 nm excitation

phonon-assisted resonant energy transfer is needed to bridge the gap between Yb^{3+} ($^2F_{5/2}$)and Tm^{3+} ($^3H_5$). As the Yb^{3+} ions relax, the ground state Tm^{3+} ion $^3H_6$ gets excited to $^3H_5$. From this energy level the Tm^{3+} ion non radiatively relaxes to $^3F_4$ energy level. The energy of the second Yb^{3+} ion is transferred to Tm^{3+}. Then the Tm^{3+} ion gets excited from $^3F_4$ to $^3F_3$. The ion non radiatively relaxes to $^3H_4$, from here the emissions $^3H_4 \rightarrow^3 F_4$ (1450 nm) is observed.

As for the ($^3F_4 \rightarrow^3 H_6$) 1650 nm emission, the $^3F_4$ energy level is populated by i) direct relaxation from $^3H_4$ in the 1450 nm emission, ii) energy transfer from Yb^{3+} ions to $^3H_5$ which non radiates to $^3F_4$. This explains why the intensity of $^3F_4 \rightarrow^3 H_6$ (1650 nm) emission peak is strong compared to the other two peaks (Savchuk et al., 2020). This is represented in the energy diagram below

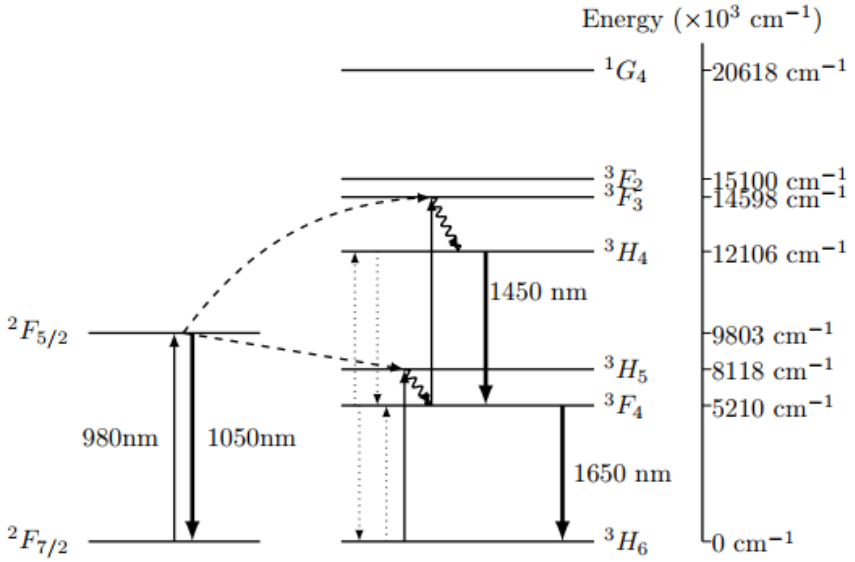

Figure 4.5: Energy level diagram of down conversion under 980 nm excitation

4.2.2 Emission spectra of the visible range.

Under 800 nm excitation a two-photon upconversion emission spectrum was observed. Three emission peaks were seen at 485 nm (blue), 650 nm (red) and 685 nm (deep red).

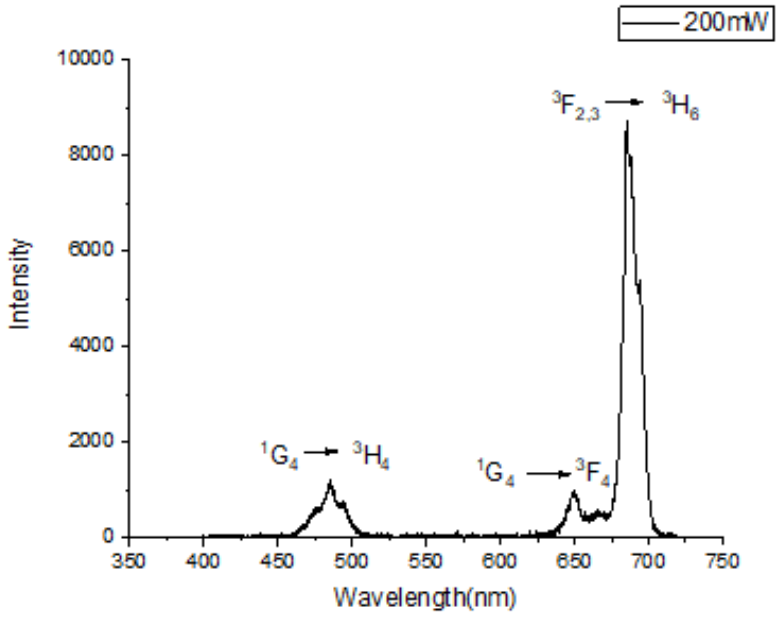

Figure 4.6: Emission spectrum of upconversion under 800 nm excitation

The upconversion process takes place through Excited state absorption(ESA). Upon excitation

with 800 nm laser, the Tm^{3+} ions absorb the photon energy and gets promoted from the ground state $^3H_6$ to $^3H_4$ (GSA), from here it non radiates to $^3H_5$ where it absorbs another photon (ESA) and rises to $^1G_4$. Two photons were absorbed making this two photon upconversion. From $^1G_4$ the Tm^{3+} ions emit radiation, $^1G_4 \rightarrow {}^3F_4$ (650 nm red emission) and $^1G_4 \rightarrow {}^3H_6$ (485 nm blue emission) as shown in the figure 4.6.

The deep red emission $^3F_3 \rightarrow {}^3H_6$ (685 nm) is attributed to the $^1G_4$ and $^3H_4$ energy levels which are populating the $^3F_3$ energy level with increasing temperature (Dussardier et al., 1995) as shown in the energy level diagram below.

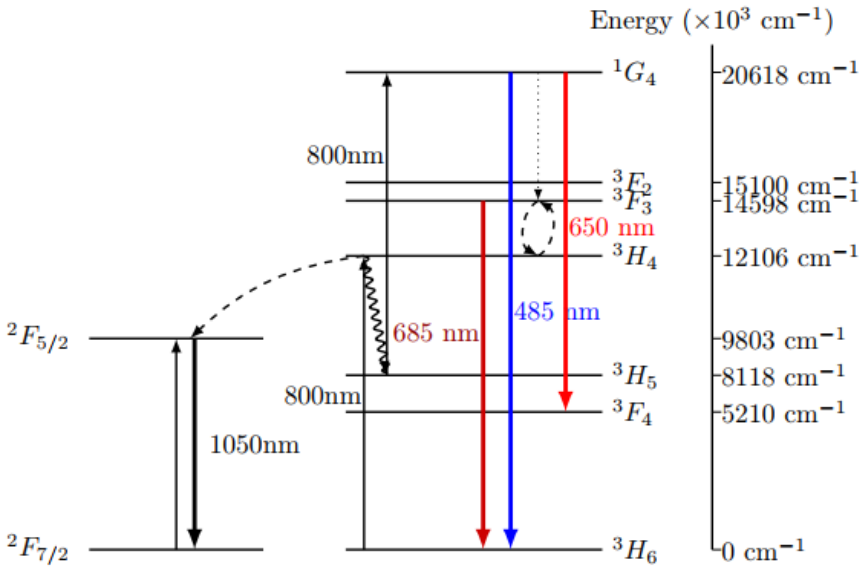

Figure 4.7: Energy level diagram of upconversion emission under 800 nm excitation

Under 980 nm excitation, three emission peaks were observed at 485 nm (blue), 650 nm (red) and, 685 nm (deep red) as was observed under 800 nm excitation. Owing to the Yb^{3+} ions strong absorption cross-section at 980 nm, the emission intensity is very high compared to the emission observed under 800 nm.

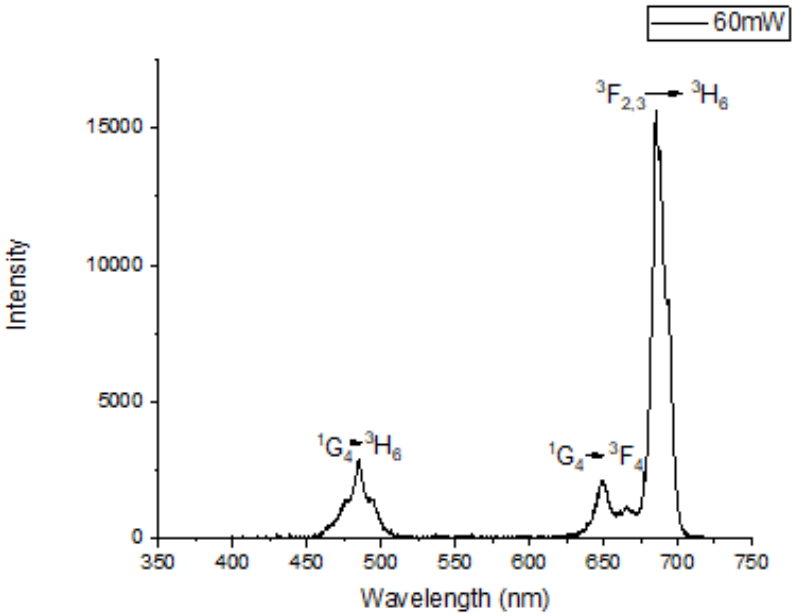

Figure 4.8: Emission spectrum of upconversion under 980 nm excitation

The process is the same as was observed during down conversion. The Yb^{3+} ions absorb energy from $^2F_{7/2}$ and excited to $^2F_{5/2}$, releasing energy and transferring to Tm^{3+} ions. The energy gap between the two elements does not perfectly match, hence phonon-assisted resonant energy transfer is needed to bridge the gap between Yb^{3+} ($^2F_{5/2}$) and Tm^{3+} ($^3H_5$).

The Tm^{3+} ions at energy level $^3H_5$ non radiatively relax to $^3F_4$. Energy from a second Yb^{3+} ion is absorbed and the Tm^{3+} ion at $^3F_4$ is promoted to $^3F_3$, from here it non radiatively relaxes to $^3H_4$, where a third energy transfer process from the Yb^{3+} ion is absorbed and the Tm^{3+} ion at $^3H_4$ rises to $^1G_4$.

The three photon energy transfer from Yb^{3+} to Tm^{3+} is conducted through energy transfer upconversion (ETU). The $^1G_4$ energy level is also populated through Excited state absorption (ESA) from $^3H_4 \rightarrow {}^1G_4$. Radiative emission takes place at $^1G_4 \rightarrow {}^3H_6$ (blue) and $^1G_4 \rightarrow {}^3F_4$ (red).

The excitation can be summarized as $^3H_6 \rightarrow {}^3H_5, {}^3H_5 \rightsquigarrow {}^3F_4, {}^3F_4 \rightarrow {}^3F_3, {}^3F_3 \rightsquigarrow {}^3H_4, and, {}^3H_4 \rightarrow {}^1G_4$ as shown in figure 4.9

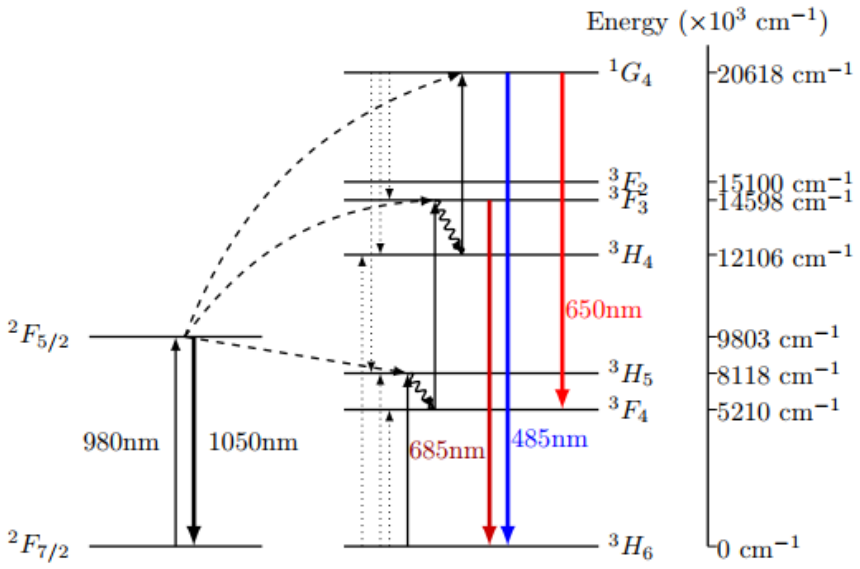

Figure 4.9: Energy level diagram of upconversion under 980 nm excitation

Possible cross relaxation(CR) processes also take place, CR paths include: CR1: $[^1G_4, ^3H_6] \rightarrow [^3F_3, ^3F_4]$, CR2: $[^1G_4, ^3H_6] \rightarrow [^3H_4, ^3H_5]$, and CR3: $[^1G_4, ^3H_6] \rightarrow [^3H_5, ^3H_4]$.

These CR process plays a role in the reduced intensity of the blue and red emission by redistributing the excitation energy among the Tm^{3+} ions

The deep red emission at 685 nm from $^3F_3$ multiplet is populated by, i) the two-photon up conversion from Yb^{3+} ($^2F_{5/2} \rightarrow {}^2F_{7/2}$) to Tm^{3+} through $^3H_6 \rightarrow {}^3H_5$, $^3H_5 \rightsquigarrow {}^3F_4$, and $^3F_4 \rightarrow {}^3F_3$, ii) possible cross relaxation from $[^1G_4, ^3H_6] \rightarrow [^3F_3, ^3F_4]$, iii) $^3H_4$ because there are thermally coupled levels, as the temperature increases $^3F_3$ can be fed by $^3H_4$ energy level (Alarcón-Fernández et al., 2022).

4.2.3 Power dependence.

The upconversion luminescence intensity spectra increased with increased power. The number of photons necessary for populating the upper emitting levels is obtained using the equation below,

$$I_{uc} \propto P^n \tag{4.2.1}$$

where, I_{uc} is the integrated UCL intensity, P is the pump power of the laser, and n represents the number of laser photons involved in the UCL process.

The value of n can be obtained from the slope of the linear fit of the logarithmic plot of the upconversion emission intensity spectra as shown in the figure below.

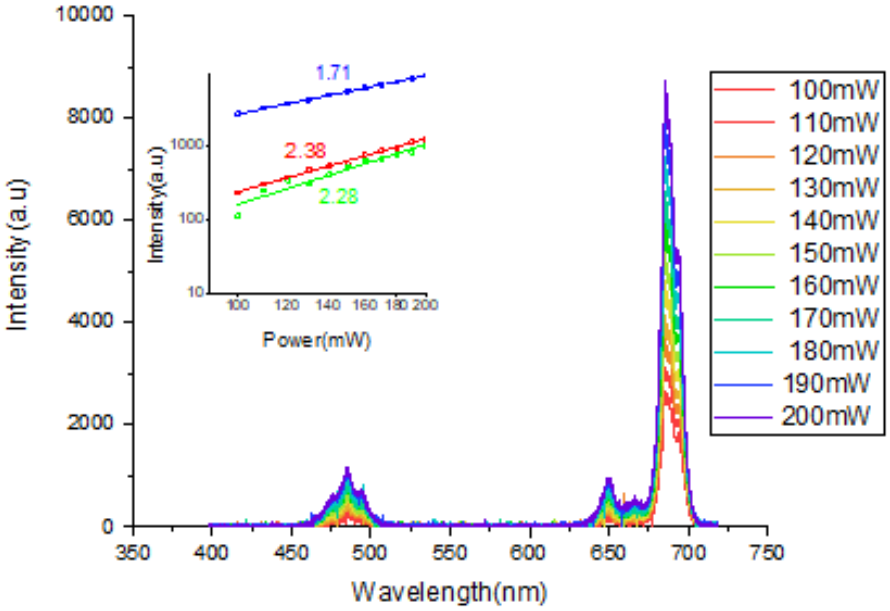

Figure 4.10: Log-Log scale of the power variation vs intensity under 800 nm excitation (upconversion).

The values of the slopes (n) measured for the blue emission (485 nm), red emission (650 nm) and deep red emissions (685 nm) were found to be 2.38, 1.7 and 2.28, and their adj.R-square was 0.99302, 0.9262 and 0.9994 respectively. This indicates that a two-photon process was responsible for the blue, red and deep red emission under 800 nm excitation.

Under 980 nm excitation a three photon process is responsible for the blue (485 nm) and red (650 nm) with slope values 2.68 and 2.76 with an adj.R-square of 0.9985 and 0.972 respectively. The deep red emission is a two photon process with slope value 1.92 and adj.R-square 0.9975 as can be seen in figure 4.11.

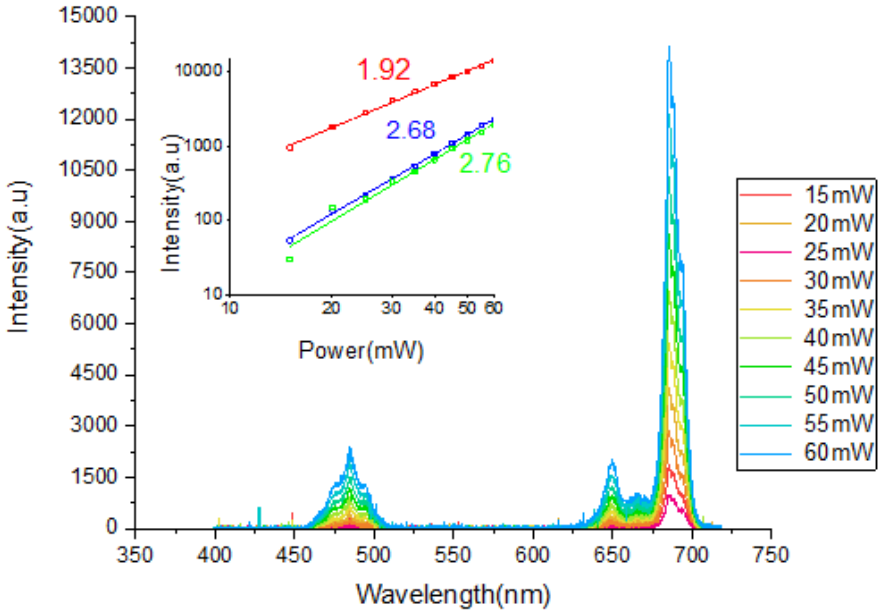

Figure 4.11: Log-Log scale of the power variation vs intensity 980 nm excitation (upconversion).

This result explains the upconversion process observed in both 980 nm and 800 nm excitation.

Power variation was also conducted in the near infrared range, under 800 nm excitation the slope was less than 1 with an adj.R-square of 0.996, 0.9987, 0.9985, for all three emissions 1050 nm, 1450 nm and 1650 nm. This result is exactly as expected because this a single photon process.

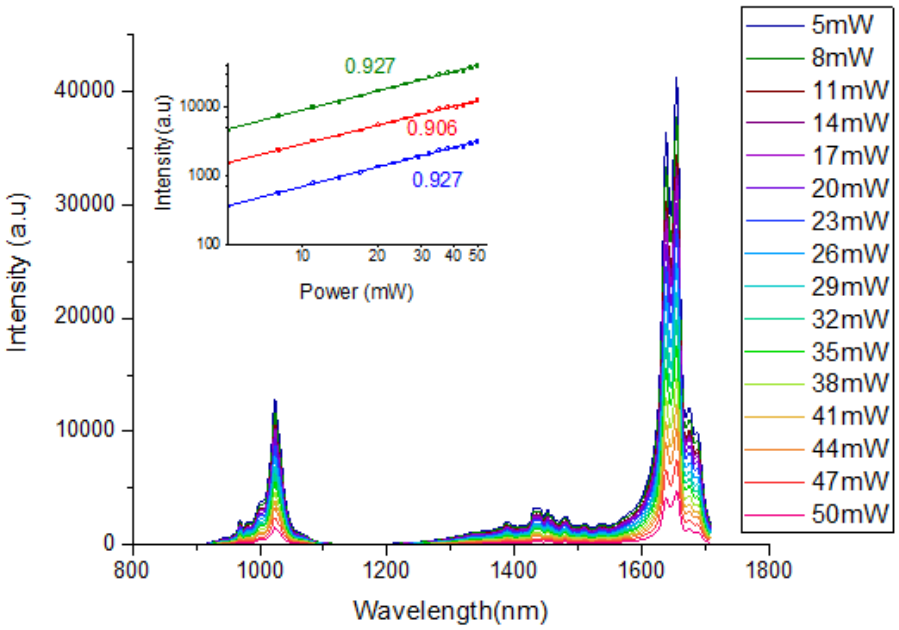

Figure 4.12: Log-Log scale of the power variation vs intensity under 800 nm excitation (down-conversion).

Under 980 nm excitation the slope of 1450 nm and 1650 nm was 1.22 ad 0.902 and an adj.R-square of 0.9994 and 0.9988 respectively. Despite the 1450 nm emission being a two photon upconversion process the slope was less than 1.5 signifying a single photon process. This is because, the decrease in the slope is determined by linear decay and excited state absorption and/or energy transfer upconversion for the depletion of the intermediate excited state in this case $^3H_4$. These intermediate excited states are long lived and act like energy reservoirs when populating higher energy levels. Hence, energy transfer upconversion occurs by a more effective single photon mechanism. As excitation power increases, the thermal effect caused by excitation at 980 nm increases the probability of the phonon assisted energy transfer process, leading to a quenching effect on the 1450 nm emission and the enhancement of the 1650 nm emission due to the improved nonradiative relaxation (Chen et al., 2015). Additionally possible power saturation and an overlap between the one photon ($^3F_4 \rightarrow {}^3H_6$) and the two photon ($^3H_4 \rightarrow {}^3F_4$) emission. As for the 1650 nm emission the process was a single photon process and the slope was approximately equal to 1 as expected.

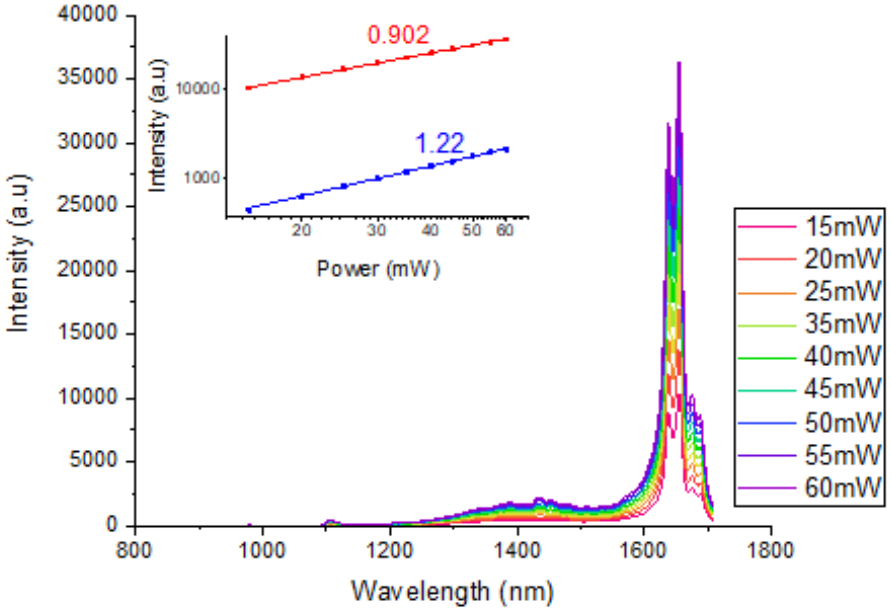

Figure 4.13: Log-Log scale of the power variation vs intensity under 980 nm excitation (down-conversion).

The fitting parameters and uncertainties are provided in Appendix 6.1.

4.3 Luminescence Thermometry

4.3.1 Downconversion.

When the sample was subjected to temperature variation in the range of 303 to 373 K, the intensity of the emission at the ${}^3F_4 \rightarrow {}^3H_6$ (1650 nm) increased with temperature while ${}^3H_4 \rightarrow {}^3F_4$ (1450 nm) and ${}^2F_{7/2} \rightarrow {}^2F_{5/2}$ (1050 nm) reduced with temperature under 800 nm excitation as shown in figure 4.14.

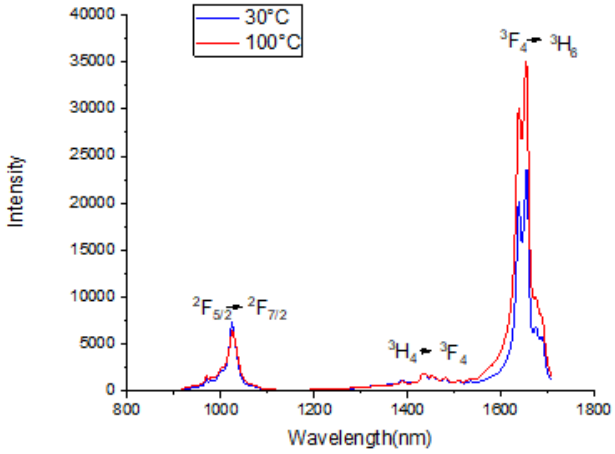

Figure 4.14: Emission intensity at $30°$C and $100°$C under 800 nm excitation

The same behavior is observed under 980 nm excitation, as the temperature increases, the intensity of the emission at the ${}^3F_4 \rightarrow {}^3H_6$ (1650 nm) increases while ${}^3H_4 \rightarrow {}^3F_4$ (1450 nm) reduces.

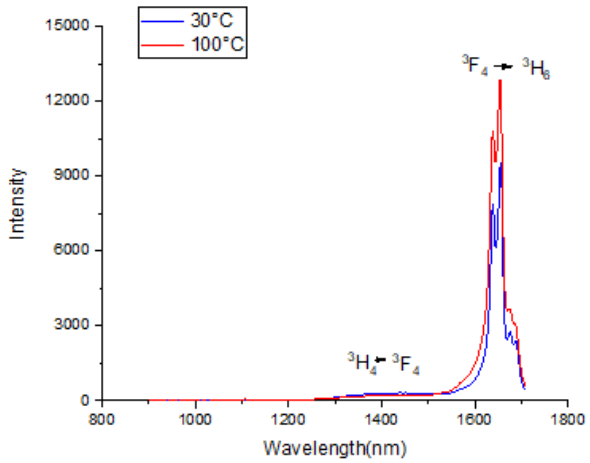

Figure 4.15: Emission intensity at $30°$ C and $100°$ C under 980 nm excitation

Although the YYbGG doped with Tm^{3+} is the same system, the three emitting levels ${}^3H_4$, ${}^3F_4$

and $^2F_{5/2}$ respond differently to temperature due to differences in their non-radiative decay rates and temperature-activated population mechanisms.

1. $^3H_4$

   At this energy level the temperature does not change the radiative transition, however it changes how much the population remains at this level long enough to emit light. The emission intensity at this level reduces as the temperature increases because the non radiative decay is dominant.

   Zhisong Xiao et al., (Xiao et al., 2008) explains how the intensity increases for $^3F_4 \rightarrow {}^3H_6$ transition is much higher than that for $^3H_4 \rightarrow {}^3F_4$ transition, evidencing quenching of the $^3H_4 \rightarrow {}^3F_4$ through cross relaxation.

   Additionally, when temperature is applied to this system , non radiative emission dominates this level, thereby decreasing the emission intensity. This phenomenon is called thermal quenching, it is the reduction of emission intensity with increasing temperature because non-radiative decay becomes faster than radiative decay.

   Furthermore, energy transfer is taking place from $^3H_4$ to $^2F_{5/2}$.

2. $^3F_4$

   This level is a low lying level with very little non radiative quenching. However, it is being populated by i) $^3H_4$ radiatively, ii) through cross relaxation process taking place at $(^3H_4,^3H_6) \rightarrow (^3F_4,^3F_4)$ and iii) thermal population redistribution, this level is low in energy, hence thermal energy makes it easier for the population to settle and stay there (Cajzl et al., 2018).

3. $^2F_{5/2}$

   Energy transfer is taking place from $^3H_4$ to $^2F_{5/2}$ (Fartas et al., 2020). As the temperature increases the population at $^3H_4$ reduces, in turn reducing the energy transfer to $^2F_{5/2}$ thereby reducing the emission intensity.

4.3.2 Upconversion.

When the sample was exposed to temperature variations from 303 to 373 K, the intensity of the emission at the $^1G_4 \rightarrow {}^3H_6$ (blue) and $^1G_4 \rightarrow {}^3F_4$ (red) gradually drops while the emission intensity of $^3F_3 \rightarrow {}^3H_6$ (685 nm) increases substantially under 800 nm excitation as shown in the figure 4.16.

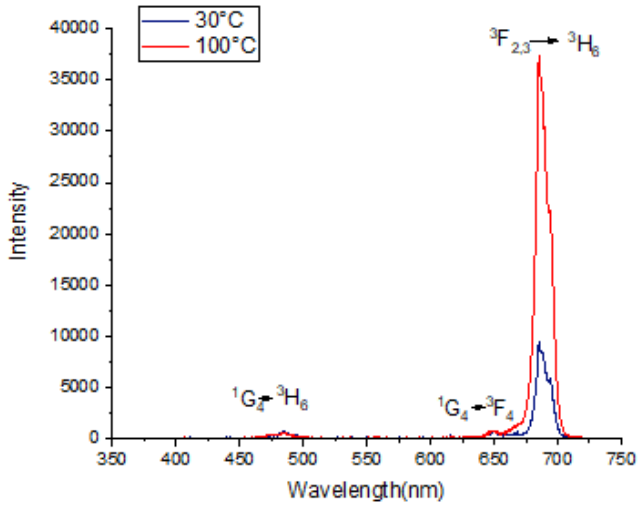

Figure 4.16: Emission intensity at 30° C and 100° C under 800 nm excitation

The same behavior is observed under 980 nm excitation

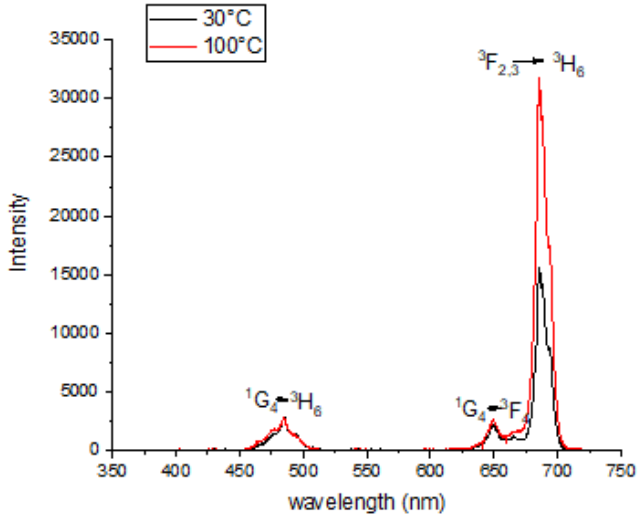

Figure 4.17: Emission intensity at 30° C and 100° C under 980 nm excitation

The emission intensity of $^3F_3 \rightarrow {}^3H_6$ (685 nm) increases because of thermal excitation from the lower adjacent energy level $^3H_4$. The energy levels $^3H_4$ and $^3F_3$ are thermally coupled energy levels with energy gap approximately 2000 cm^{-1}, hence, thermal excitation increases the population of $^3F_3$ thereby increasing the emission intensity (Upadhyay et al., 2023).

The intensity of the emission at the $^1G_4 \rightarrow {}^3H_6$ (blue) and $^1G_4 \rightarrow {}^3F_4$ (red) reduces because non radiative transitions are dominant in these levels and these transitions increase with temperature (Li et al., 2021; Savchuk et al., 2020).

4.3.3 Luminescence Intensity ratio and Relative sensitivity.

Downconversion

The intensity ratio of I_{1650}/I_{1050} under 800 nm excitation was plotted in figure 4.18, The non thermally coupled levels $^3F_4$ and $^2F_{5/2}$ were utilized for luminescence intensity ratio (LIR). In this work, instead of solving the complex system of rate equations that describes this luminescence process, we adopted the use of empirical curves to model the LIR versus temperature behavior. The experimental data was plotted and fitted using the following linear equation

$$LIR = \frac{I_{1650}}{I_{1050}} = a + bT \tag{4.3.1}$$

Where a and b are constants whose values can be found by fitting the experimental data and T denotes the absolute temperature from 303 to 373 K.

The absolute sensitivity is given by

$$S_a = \frac{d(LIR)}{dT} = b \tag{4.3.2}$$

Therefore, the relative sensitivity is given by

$$S_r = \frac{b}{LIR} \tag{4.3.3}$$

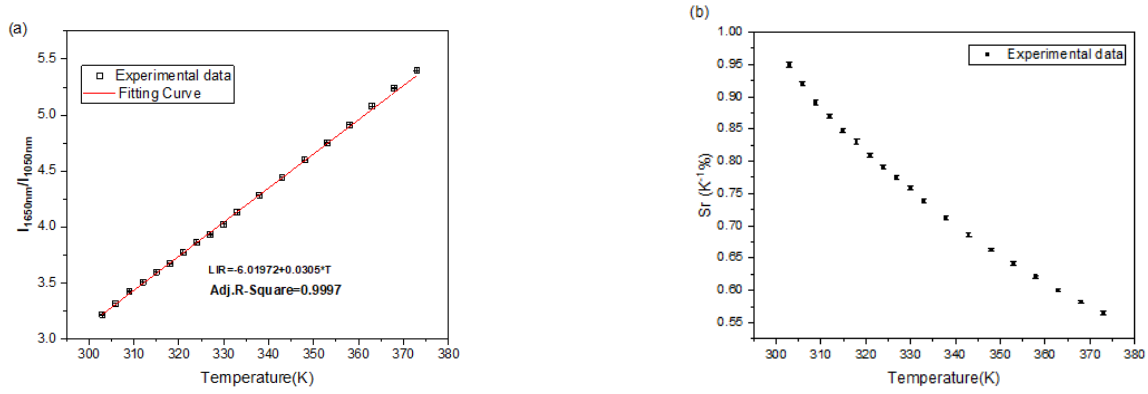

Figure 4.18: LIR and relative sensitivity under 800 nm excitation: (a) intensity ratio of I_{1650}/I_{1050} (b) relative sensitivity of ratio I_{1650}/I_{1050}

It can be seen that the relative sensitivity reduces as the temperature increases, this sensor is best suited for cryogenic temperature applications.

The intensity ratio of I_{1650}/I_{1450} under 800 nm excitation was plotted. The non thermally coupled levels $^3F_4$ and $^3H_4$ were used in the calculation of the luminescence intensity ratio (LIR). The experimental data was plotted and fitted in figure 4.19 using the following exponential equation.

$$LIR = \frac{I_{1650}}{I_{1450}} = Y_0 + A \times exp(R_0 T) \tag{4.3.4}$$

where Y_0, A and R_0 are empirical constants whose values can be found by fitting the experimental data and T denotes the absolute temperature from 303 to 373 K.

The absolute sensitivity is given by

$$S_a = \frac{d(LIR)}{dT} = AR_0 \times exp(R_0 T) \tag{4.3.5}$$

Therefore, the relative sensitivity is given by

$$S_r = \frac{AR_0 \times exp(R_0 T)}{LIR} \tag{4.3.6}$$

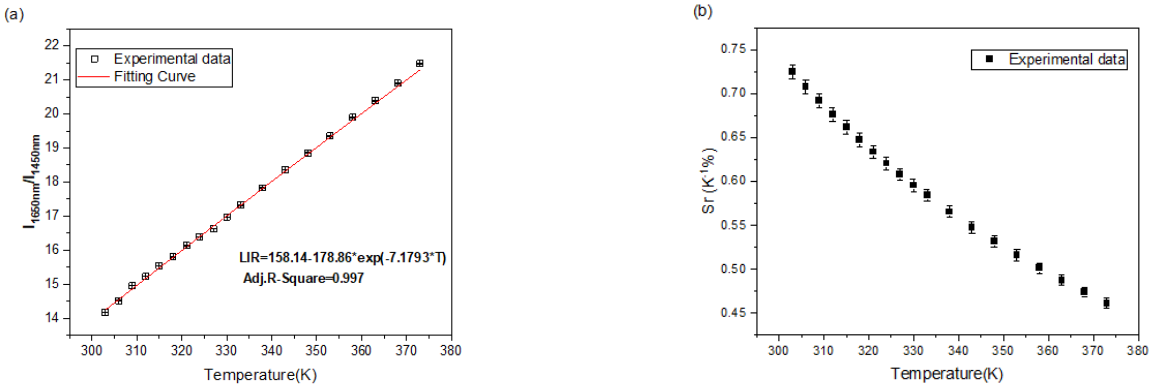

Figure 4.19: LIR and relative sensitivity under 800 nm excitation: (a) intensity ratio of I_{1650}/I_{1450} (b) relative sensitivity of ratio I_{1650}/I_{1450}

From the fig 4.19 the relative sensitivity reduces as the temperature increases, this shows that this sensor is also suitable for cryogenic temperature application. The relative sensitivity is lower than that observed in 4.18, this is because the I_{1650}/I_{1050} ($^3F_4/^2F_{5/2}$) ratio involves inter-ionic energy transfer processes between Tm^{3+} and Yb^{3+}. The I_{1650}/I_{1450} ($^3F_4/^3H_4$) ratio is attributed to the strong multiphonon quenching of the $^3H_4$ level at elevated temperatures hence having a relative sensitivity of $0.72K^{-1}$%.

The intensity ratio of I_{1650}/I_{1450} under 980 nm excitation was plotted in figure 4.20. Non thermally coupled levels $^3F_4$ and $^3H_4$ were employed in the calculation of the luminescence intensity ratio (LIR). The data was adjusted using the exponential equation 4.3.4 as was done under 800 nm excitation using the same LIR ratio. LIR ratio and relative sensitivity are shown in figure 4.20.

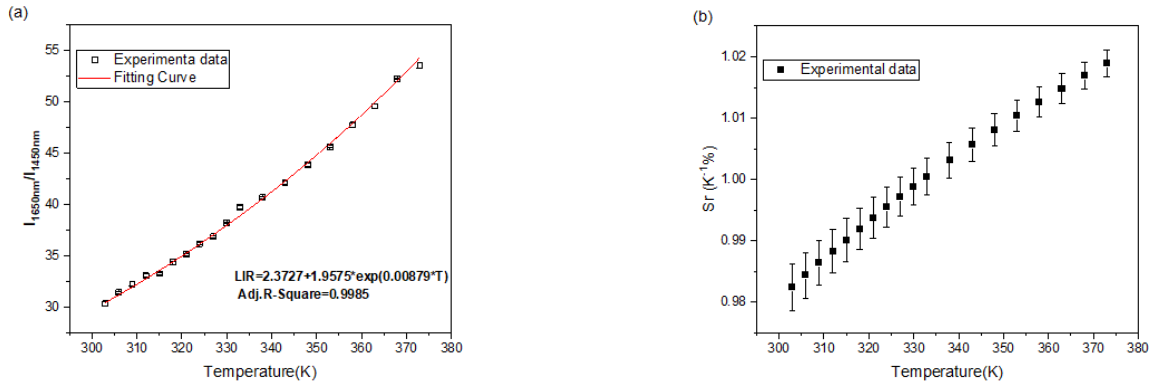

Figure 4.20: LIR and relative sensitivity under 980 nm excitation: (a) intensity ratio of I_{1650}/I_{1450} (b) relative sensitivity of ratio I_{1650}/I_{1450}

The figure 4.20 shows the relative sensitivity increasing with increasing temperature, this means this sensor is suitable for high temperature applications. This behavior of the relative sensitivity is different when compared with the results shown in figure 4.19. This happens because although the same pair of levels have been used in both cases, the differences of the excitation wavelengths lead to distinct excitation processes.

Upconversion

The intensity ratio of I_{685}/I_{650} under 800 nm excitation was plotted in figure 4.21 The non thermally coupled levels $^3F_3$ and $^1G_4$ were utilized for luminescence intensity ratio (LIR). The data was fitted using the exponential equation 4.3.4

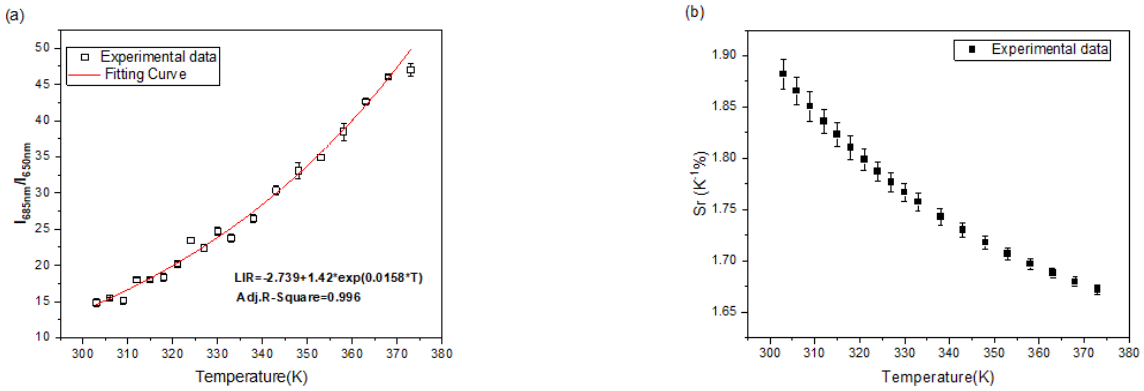

Figure 4.21: LIR and relative sensitivity under 800 nm excitation: (a) Intensity ratio of I_{685}/I_{650} (b) relative sensitivity of ratio I_{685}/I_{650}

This sensor is best suited for cryogenic temperature applications because the relative sensitivity reduces with increasing temperature.

Following the same procedure. The intensity ratio of I_{685}/I_{485} under 800 nm excitation was plotted in figure 4.22, The non thermally coupled levels $^3F_3$ and $^1G_4$ were employed in the calculation of the luminescence intensity ratio (LIR). The data was modeled using the exponential equation 4.3.4.

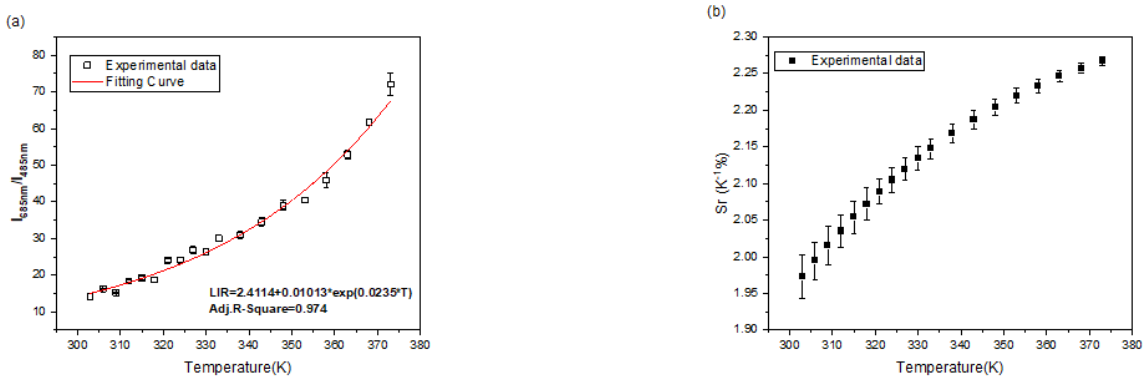

Figure 4.22: LIR and relative sensitivity under 800 nm excitation: (a) intensity ratio of I_{685}/I_{485} (b) relative sensitivity of ratio I_{685}/I_{485}

This sensor is best suited for high temperature applications. The relative sensitivity increases

with increasing temperature.

Under 980 nm excitation the LIR I_{685}/I_{650}, related to the non thermally coupled levels $^3F_3$ and $^1G_4$ was investigated. In figure 4.23, it is presented this LIR data and its corresponding fitting curve (4.3.4). The relative sensitivity for this sensor system was calculated using equations 4.3.5 and 4.3.6. The result is presented in fig 4.23

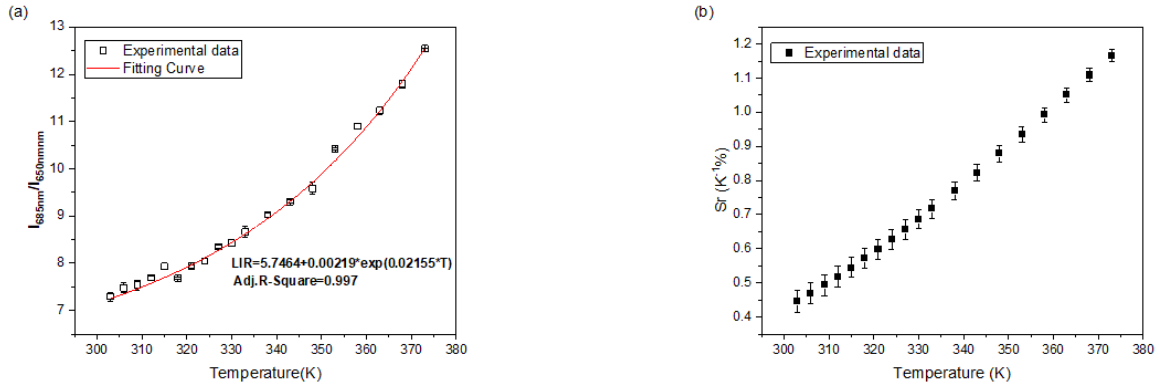

Figure 4.23: LIR and relative sensitivity under 980 nm excitation: (a) intensity ratio of I_{685}/I_{650} (b) relative sensitivity of ratio I_{685}/I_{650}

This sensor is best suited for high temperature applications. The relative sensitivity increases with increasing temperature.

At last, the LIR I_{685}/I_{485} was investigated for 980 nm excitation wavelength. This ratio is also based on the non thermally coupled levels $^3F_3$ and $^1G_4$. The result is presented in fig 4.24. Again, the data presented a approximately exponential growth with temperature and was fitted with equation 4.3.4. In fig. 4.24 and the relative sensitivity of this LIR was calculated using equations 4.3.5 and 4.3.6.

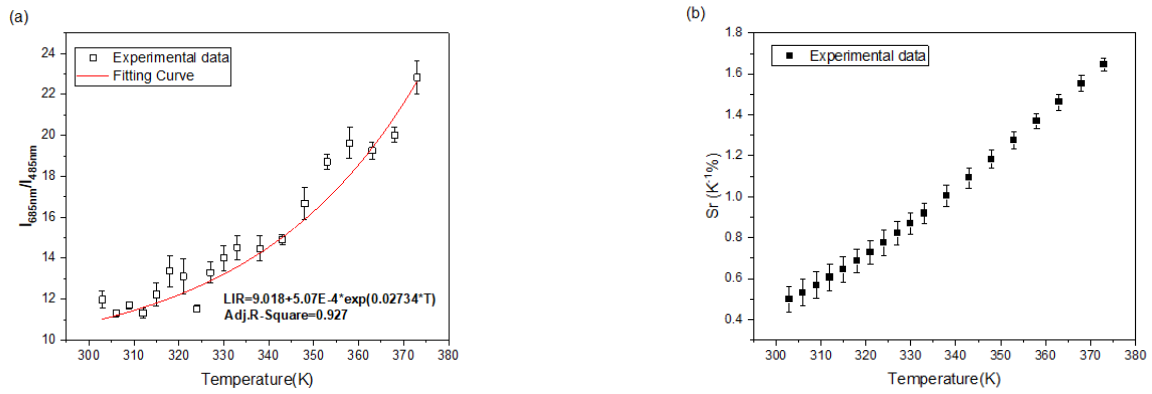

Figure 4.24: LIR and relative sensitivity under 980 nm excitation: (a) Intensity ratio of I_{685}/I_{485} (b) relative sensitivity of ratio I_{685}/I_{485}

This sensor is best suited for high temperature applications. The relative sensitivity increases with increasing temperature.

It is worth mentioning that, although the LIR methodologies of the ratios I_{685}/I_{650} and I_{685}/I_{485} employ transitions from the same emitting levels $^1G_4$ (650 and 485 nm) and $^3F_3$ (685 nm), the empirical fitting parameters are not the same, even when you use the same excitation path. This is happening because the emission bands from both emitters are overlapped. In this scenario, it is more appropriate to describe the LIR using the equation:

$$LIR(T) = I_U/I_L = \frac{(a_2 I_2 + b_1 I_1)}{(a_1 I_2 + b_2 I_1)}, \tag{4.3.7}$$

where I_2 is the intensity emission from the $^1G_4$ level and I_1 is the intensity from the $^3F_3$ level. Using this approach, the numerator refers to the overlap between the emissions that contributes to the intensity measure at 685 nm, while the denominator is the sum of the contributions from both levels for the 650 nm. The a and b coefficients represents the fraction of each emission to the overall intensity.

Nevertheless , the emission at 485 nm present a different (if any) overlap between the emissions from both $^1G_4$ and $^3F_3$ levels. Hence, the LIR in this case can be described as

$$LIR(T) = I_U/I_L = \frac{(a_2 I_2 + b_1 I_1)}{B_2 I_1} = \frac{a_2}{B_2} \times \frac{I_2}{I_1} + b_{12}. \tag{4.3.8}$$

As I_1 and I_2 varies differently with temperature, these two LIR's should present distinct temperature behaviors (Laia et al., 2020).

The fitting parameters and uncertainties are provided in Appendix 6.2.

4.4 Comparison with other temperature sensors

To compare the thermometry capacity of YYbGG doped with Tm^{3+}, the relevant parameters from other research are listed in the table 4.1. The similarities and differences of the Tm^{3+} and Yb^{3+} doped samples listed in the table are as follows, The similarities were:

- Both studies used the LIR method on non-thermally coupled levels.
- Temperature ranges in both cases started from no less than 25 °C.

The differences were:

- Most previous studies, such as Y_2O_3, $LaVO_4$, and $GdVO_4$, used LIR method on both thermally coupled and non-thermally coupled levels.
- Despite using the LIR method the energy levels and ratios differed compared to the current work.
- In most previous studies, the temperature range exceeded 373 K, whereas in the current work the experiments were conducted only up to 373 K.
- The comparison table only considers 980 nm excitation and upconversion, while the current work uses both 800 nm and 980 nm excitation and also considers downconversion.

Table 4.1: Summary of luminescence thermometry parameters for Tm^{3+}/Yb^{3+} materials.

Material	Temp. Range (K)	Excitation (nm)	Wavelength Ratio	S_{rel} (% K^{-1})	Ref.
$NaYF_4$:Tm^{3+}/Yb^{3+}	297–565	980	I_{692}/I_{650}	2.7	(Li et al., 2021)
Y_2O_3:Tm^{3+}/Yb^{3+}	303–573	980	I_{684}/I_{490}	1.51	(Chen et al., 2018a)
$LiLa(MoO_4)_2$:Tm^{3+}/Yb^{3+}	300–543	980	I_{700}/I_{650}	3.85	(Hu et al., 2016)
Bi_2Wo_6:Tm^{3+}/Yb^{3+}	298–573	980	I_{705}/I_{650}	3.78	(Xiakeer et al., 2023)
YVO_4:Tm^{3+}/Yb^{3+}	300–1000	980	I_{700}/I_{800}	2.1	(Runowski et al., 2020)
NaY_2F_7:Tm^{3+}/Yb^{3+}	300–567	980	I_{678}/I_{700}	1.6	(Chen et al., 2020)
$Ba_3La(P0_4)_3$:Tm^{3+}/Yb^{3+}	303–503	980	I_{690}/I_{792}	2.11	(Cao et al., 2018)
$KLuF_4$:Tm^{3+}/Yb^{3+}	303–503	980	I_{690}/I_{795}	1.0	(Min et al., 2017)
YF_3:Tm^{3+}/Yb^{3+}	298–778	980	I_{700}/I_{776}	2.80	(Suo et al., 2017)
YAG:Tm^{3+}/Yb^{3+}	303–733	976	I_{683}/I_{782}	2.30	(Yu et al., 2017)
$LaVo_4$:Tm^{3+}/Yb^{3+}	300–653	980	I_{700}/I_{475}	0.89	(Upadhyay et al., 2023)
$GdVo_4$:Tm^{3+}/Yb^{3+}	300–653	980	I_{700}/I_{475}	1.179	(Upadhyay et al., 2023)
YGG:Tm^{3+}/Yb^{3+}	303–373	980	I_{685}/I_{485}	1.64	This work
YGG:Tm^{3+}/Yb^{3+}	303–373	980	I_{685}/I_{650}	1.66	This work
YGG:Tm^{3+}/Yb^{3+}	303–373	800	I_{685}/I_{485}	2.26	This work
YGG:Tm^{3+}/Yb^{3+}	303–373	800	I_{685}/I_{650}	1.88	This work
YGG:Tm^{3+}/Yb^{3+}	303–373	800	I_{1650}/I_{1050}	0.94	This work
YGG:Tm^{3+}/Yb^{3+}	303–373	800	I_{1650}/I_{1450}	0.72	This work
YGG:Tm^{3+}/Yb^{3+}	303–373	980	I_{1650}/I_{1450}	1.02	This work

From the table, it can be seen that the relative sensitivity in previous works ranged from 0.89 to 3.85. In the current work, considering both 800 nm and 980 nm excitation, as well as downconversion and upconversion across different energy level ratios, the relative sensitivity ranged from 0.72 to 2.26. This demonstrates that YYbGG-Tm is an excellent temperature sensor and can be effectively used under various conditions.

5. Conclusion and Perspectives

5.1 Conclusion

This study focussed on observing the luminescence of YYbGG doped with thulium in the infrared and visible wavelengths. Two processes, downconversion and upconversion were observed under 800 nm and 980 nm excitation. Additionally power variation and temperature variation experiments were performed on the sample.

The sample was observed to have three peaks in both the visible; 485 nm (blue), 650 nm (red) and, 685 nm (deep red) and near infrared wavelengths; 1050 nm, 1450 nm and, 1650 nm. Luminescence intensity ratio was used to determine the relative sensitivities of the six peaks in the temperature range 303 to 373K. The relative sensitivity ranged from 0.72 to 1.02 % K^{-1} during downconversion, and 1.64 to 2.26 % K^{-1} during upconversion.

It is therefore concluded that this YYbGG - Tm^{3+} is a promising luminescence temperature probe, which can be used in upconversion and downconversion experiments with either 800 nm or 980 nm laser excitation.

5.2 Perspectives

5.2.1 Temperature range.

The temperature range used in this study was from 303 K to 333 K in intervals of 3 and from 333 K to 373 K in intervals of 5. Since the relative sensitivity under 980 nm excitation increased with temperature and the emission spectra of the $^3F_4 \rightarrow\ ^3H_6$ (1650 nm) during downconversion and the deep red emission $^3F_3 \rightarrow\ ^3H_6$ (685 nm) during upconversion under both 800 nm and 980 nm laser excitation increased, also apart from $I_{685/485}$ ratio under 800 nm excitation the rest of the ratios under this excitation wavelength have sensor schemes more sensitive to lower temperatures. It is therefore suggested in future works to monitor the behavior of the Tm^{3+} - doped YYbGG crystals with temperature higher than 373 K and lower than 303 K.

5.2.2 Particle size.

The application of temperature probes is also determined by the size of the lanthanide particle size constraints. By decreasing the size of the temperature probe from micro to nano-particles , it is possible to incorporate probes in other catalystic particles (Geitenbeek, 2018). Both micro and nano-particles are good thermometry probes however, nanoparticles allow higher spatial resolution that is, they can access temperature in much smaller regions (Pudovkin et al., 2019). Tm^{3+} -doped YYbGG crystals once reduced to nano size would be a great thermometric probe in biological applications.

References

Søren Dyøe Agger and Jørn Hedegaard Povlsen. Emission and absorption cross section of thulium doped silica fibers. *Optics Express*, 14:50–57, 2006. doi: 10.1364/OPEX.14.000050. URL https://doi.org/10.1364/OPEX.14.000050.

Carlos Alarcón-Fernández, Carlos Zaldo, and Concepción Cascales. Yb^{3+}, Er^{3+}, Tm^{3+} co-doped $\beta' Gd_2(MoO_4)_3$ for high-sensitivity luminescence thermometry spanning from 300 to 890 k. *Journal of Alloys and Compounds*, 913:165180, 2022. doi: 10.1016/j.jallcom.2022.165180. URL https://doi.org/10.1016/j.jallcom.2022.165180.

Leonardo Vieira Albino, Agustín Delendatti, Fábio José Caixeta, Thiago Augusto Lodi, Douglas Faza Franco, Camila Batista Pinto, Javier Alcides Ellena, and Marcelo Nalin. Innovative synthesis of Tm^{3+}/Er^{3+}-doped yb-ygg single crystals for upconversion-based white light emission. *Ceramics International*, 51(12):16700–16709, 2024. doi: 10.1016/j.ceramint.2024.11.480. URL https://doi.org/10.1016/j.ceramint.2024.11.480.

Márcio A. R. C. Alencar, Glauco S. Maciel, and Cid B. de Araújo. Er^{3+} doped $BaTiO_3$ nanocrystals for thermometry: Influence of nanoenvironment on the sensitivity of a fluorescence based temperature sensor. *Appl. Phys. Lett.*, 84:4753–4755, 2004. doi: 10.1063/1.1760882. URL https://doi.org/10.1063/1.1760882.

Santanu Banerjee, G. Ajith Kumar, Thomas J. Emge, Richard E. Riman, and John G. Brennan. Thiolate-bound thulium compounds: Synthesis, structure, and nir emission. *Chem. Mater.*, 20 (13):4367–4373, 2008. doi: 10.1021/cm800627f. URL https://doi.org/10.1021/cm800627f.

Elixir William Barrera Bello. *Lanthanide-based dielectric nanoparticles for upconversion luminescence*. PhD thesis, Universitat Rovira i Virgili, 2013.

Dong Biao, Song Hongwei, Qin Ruifei, Bai Xue, Lu Shaozhe, Ren Xinguang, Pan Guohui, Zhang Hui, Wang Fang, and Fan Libo. Upconversion white light devices: Ln^{3+}-tridoped $NaYF_4$ nanoparticles and pvp modified films. *Journal of Nanoscience and Nanotechnology*, 8(8): 3921–3925, 2008. doi: 10.1166/jnn.2008.182. URL https://doi.org/10.1166/jnn.2008.182.

Antonio C. Brandão-Silva, Maria A. Gomes, Zélia S. Macedo, Jhon F. M. Avila, José J. Rodrigues Jr, and Márcio A. R. C. Alencar. Multiwavelength fluorescence intensity ratio nanothermometry: High sensitivity over a broad temperature range. *J. Phys. Chem. C*, 122(35):20459–20468, 2018. doi: 10.1021/acs.jpcc.8b05345. URL https://doi.org/10.1021/acs.jpcc.8b05345.

Jakub Cajzl, Pavel Peterka, Maciej Kowalczyk, Jan Tarka, Grzegorz Soboń, Jarosław Sotor, Jan Aubrecht, Pavel Honzátko, and Ivan Kasík. Thulium-doped silica fibers with enhanced fluorescence lifetime and their application in ultrafast fiber lasers. *Fibers*, 6:66, 2018. doi: 10.3390/fib6030066. URL https://doi.org/10.3390/fib6030066.

Jiafeng Cao, Jia Zhang, and Xiaowei Li. Upconversion luminescence of $Ba_3La(PO_4)_3$:Yb^{3+}+Er^{3+}/Tm^{3+} phosphors for optimal temperature sensing. *Applied Optics*, 57(6):1345–1350, 2018. doi: 10.1364/AO.57.001345. URL https://doi.org/10.1364/AO.57.001345.

Renato Grigolon Capelo, Clément Strutynski, Gregory Gadret, Frédéric Désévédavy, Frédéric Smektala, and Danilo Manzani. Blue upconversion emission of $Nd^{3+}/Tm^{3+}/Yb^{3+}$ triply doped aluminophosphate optical fibers. *ACS Appl. Opt. Mater.*, 2:2501–2508, 2024. doi: 10.1021/acsaom.4c00348. URL https://doi.org/10.1021/acsaom.4c00348.

Elisa Carrasco, Blanca del Rosal, Francisco Sanz-Rodríguez, Ángeles Juarranz de la Fuente, Patricia Haro Gonzalez, Ueslen Rocha, Kagola Upendra Kumar, Carlos Jacinto, José García Solé, and Daniel Jaque. Intratumoral thermal reading during photo-thermal therapy by multifunctional fluorescent nanoparticles. *Advanced Functional Materials*, 25(4):615–626, 2015. doi: 10.1002/adfm.201403653. URL https://doi.org/10.1002/adfm.201403653.

Ruitao Chai, Hongzhou Lian, Zhiyao Hou, Cuimiao Zhang, Chon Peng, and Jun Lin. Preparation and characterization of upconversion luminescent $NaYF_4 : Yb^{3+}, Er^{3+}, (Tm^{3+})$/PMMA bulk transparent nanocomposites through in situ photopolymerization. *Journal of Physical Chemistry C*, 114(1):610–616, 2010. doi: 10.1021/jp909180s. URL https://doi.org/10.1021/jp909180s.

Dev K. Chatterjee, Abdul J. Rufaihah, and Yong Zhang. Upconversion fluorescence imaging of cells and small animals using lanthanide doped nanocrystals. *Biomaterials*, 29(7):937–943, 2008. doi: 10.1016/j.biomaterials.2007.10.051. URL https://doi.org/10.1016/j.biomaterials.2007.10.051.

Daqin Chen, Yuansheng Wang, Kelu Zheng, Tailiang Guo, Yunlong Yu, and Ping Huang. Bright upconversion white light emission in transparent glass ceramic embedding $Tm^{3+}/Er^{3+}/\ Yb^{3+}$: $\beta - YF_3$ nanoparticles. *Applied Physics Letters*, 91:251903, 2007. doi: 10.1063/1.2825285. URL https://doi.org/10.1063/1.2825285.

Gengxu Chen, Chengjie Ding, E. Wu, Botao Wu, Ping Chen, Xueting Ci, Yan Liu, Jianrong Qiu, and Heping Zeng. Tip-enhanced upconversion luminescence in Yb^{3+}–Er^{3+} codoped $NaYF_4$ nanocrystals. *J. Phys. Chem. C*, 119:22604–22610, 2015. doi: 10.1021/acs.jpcc.5b04387. URL https://doi.org/10.1021/acs.jpcc.5b04387.

Guangrun Chen, Ruoshan Lei, Huanping Wang, Feifei Huang, Shilong Zhao, and Shiqing Xu. Temperature-dependent emission color and temperature sensing behavior in Tm^{3+}/Yb^{3+}:Y_2O_3 nanoparticles. *Optical Materials*, 77:233–239, 2018a. doi: 10.1016/j.optmat.2018.01.039. URL https://doi.org/10.1016/j.optmat.2018.01.039.

Guanying Chen, Hailong Qiu, Paras N. Prasad, and Xiaoyuan Chen. Upconversion nanoparticles: Design, nanochemistry, and applications in theranostics. *Chemical Reviews*, 114(10):5161–5214, 2025. doi: 10.1021/cr400425h. URL https://doi.org/10.1021/cr400425h.

Sunyuezi Chen, Weihui Song, Jiangkun Cao, Fangfang Hu, and Hai Guo. Highly sensitive optical thermometer based on fir technique of transparent NaY_2F_7:Tm^{3+}/Yb^{3+} glass ceramic. *Journal of Alloys and Compounds*, 825:154011, 2020. doi: 10.1016/j.jallcom.2020.154011. URL https://doi.org/10.1016/j.jallcom.2020.154011.

Zikun Chen, Bo Wang, Xiaoshuang Li, Lei Kang, Yeqing Chen, Yan Chen, Hongyang Sun, and Qingguang Zeng. Facile synthesis of self-activated oxyfluorotungstate phosphor with high QE

and its thermal quenching. *Journal of Alloys and Compounds*, 770:559–563, 2018b. doi: 10.1016/j.jallcom.2018.08.126. URL https://doi.org/10.1016/j.jallcom.2018.08.126.

Ziyu Chen, Hang Zhu, Jiajie Qian, Zhenxiong Li, Xiameng Hu, Yuao Guo, Yuting Fu, Huazhong Zhu, Wei Nai, Zan Yang, Dan Yang, and Liling Zhou. Rare earth ion doped luminescent materials: A review of up/down conversion luminescent mechanism, synthesis, and anti-counterfeiting application. *Photonics*, 10:1014, 2023. doi: 10.3390/photonics10091014. URL https://doi.org/10.3390/photonics10091014.

Antariksha Das. *Towards a Long-Lived and Efficient Photonic Quantum Memory in a Thulium-Doped Crystal*. PhD thesis, Technische Universiteit Delft, 2022.

Jacob H. Davidson, Dorian Oser, and Wolfgang Tittel. Optical properties of yttrium gallium garnet. *arXiv*, 2203.01689, 2022. doi: 10.48550/arXiv.2203.01689. URL https://doi.org/10.48550/arXiv.2203.01689.

Matthew J. Dejneka, Alexander Streltsov, Santona Pal, Anthony G. Frutos, Christy L. Powell, Kevin Yost, Po Ki Yuen, Uwe Müller, and Joydeep Lahiri. Rare earth-doped glass microbarcodes. *Science and Technology Division, Corning Incorporated, Corning, NY*, 100(2):389–393, 2003. doi: 10.1073/pnas.0236044100. URL https://doi.org/10.1073/pnas.0236044100.

Michel J. F. Digonnet. *Rare-Earth-Doped Fiber Lasers and Amplifiers, Revised and Expanded*. CRC Press, 2001.

Miroslav D. Dramićanin. Trends in luminescence thermometry. *J. Appl. Phys.*, 128:040902, 2020. doi: 10.1063/5.0014825. URL https://doi.org/10.1063/5.0014825.

B. Dussardier, J. Wang, D. C. Hanna, and D. N. Payne. Spectroscopy and cw 2-photon up-conversion in Tm^{3+}-doped $ZnCl_2$-based glass. *Optical Materials*, 4(5):565–573, 1995. doi: 10.1016/0925-3467(95)00008-9. URL https://doi.org/10.1016/0925-3467(95)00008-9.

Svetlana V. Eliseeva and Jean-Claude G. Bünzli. Rare earths: jewels for functional materials of the future. *New Journal of Chemistry*, 35:1165–1176, 2011. doi: 10.1039/C0NJ00969E. URL https://doi.org/10.1039/C0NJ00969E.

R. Fartas, M. Diaf, I. R. Martin, F. Paz-Buclatin, and J. P. Jouart. Near-infrared and upconversion luminescence of Tm^{3+}-Yb^{3+} codoped CdF_2 single crystals. *Journal of Luminescence*, 228: 117594, 2020. doi: 10.1016/j.jlumin.2020.117594. URL https://doi.org/10.1016/j.jlumin.2020.117594.

B. Faure, W. Blanc, B. Dussardier, and G. Monnom. Improvement of the Tm^{3+}:$^3H_4$ level lifetime in silica optical fibres by lowering the local phonon energy. *Journal of Non-Crystalline Solids*, 353:2767–2773, 2007. doi: 10.1016/j.jnoncrysol.2007.05.025. URL https://doi.org/10.1016/j.jnoncrysol.2007.05.025.

Tardieu François, Reymond Matthieu, Hamard Philippe, Granier Christine, and Muller Bertrand. Turgor, cell growth and leaf development: Spatial distributions of expansion rate, cell division rate and cell size in maize leaves — a synthesis of the effects of soil water status, evaporative

demand and temperature. *Journal of Experimental Botany*, 51(350):1505, 2000. doi: 10.1093/jexbot/51.350.1505. URL https://doi.org/10.1093/jexbot/51.350.1505.

G. Frith, D. G. Lancaster, and S. D. Jackson. 85 w tm^{3+}-doped silica fibre laser. *Electronics Letters*, 41(12):687–688, 2005. doi: 10.1049/el:20051207. URL https://doi.org/10.1049/el:20051207.

H. Gebavi, D. Milanese, R. Balda, S. Chaussedent, M. Ferrari, J. Fernandez, and M. Ferraris. Spectroscopy and optical characterization of thulium doped tzn glasses. *Journal of Physics D: Applied Physics*, 43(13):135104, 2010. doi: 10.1088/0022-3727/43/13/135104. URL https://10.1088/0022-3727/43/13/135104.

Robin Gabriël Geitenbeek. *Luminescence Thermometry: Fundamentals and Applications*. PhD thesis, Universiteit Utrecht, 2018.

Lauren Guillemot, Pavel Loiko, Jean-Louis Doulan, Alain Braud, and Patrice Camy. Excited-state absorption in thulium-doped materials in the near-infrared. *Optics Express*, 30(18):31669–31684, 2022. doi: 10.1364/OE.460176. URL https://doi.org/10.1364/OE.460176.

P. Haro-González, L. Martínez Maestro, M. Trevisani, S. Polizzi, D. Jaque, J. García Solé, and M. Bettinelli. Evaluation of rare earth doped silica sub-micrometric spheres as optically controlled temperature sensors. *Journal of Applied Physics*, 112:054702, 2012. doi: 10.1063/1.4751349. URL https://doi.org/10.1063/1.4751349.

M. A. Hernández-Rodriguez, A. D. Lozano-Gorrín, V. Lavín, U. R. Rodríguez-Mendoza, and I. R. Martín. Yttrium orthoaluminate nanoperovskite doped with Tm^{3+} ions as upconversion optical temperature sensor in the near-infrared region. *Optics Express*, 25(22):27845–27856, 2017. doi: 10.1364/OE.25.027845. URL https://doi.org/10.1364/OE.25.027845.

C. W. Hoyt and M. Sheik-Bahae. Observation of anti-stokes fluorescence cooling in thulium-doped glass. *Physical Review Letters*, 85:3600, 2000. doi: 10.1103/PhysRevLett.85.3600. URL https://doi.org/10.1103/PhysRevLett.85.3600.

Wenjie Hu, Fangfang Hu, Xinyue Li, Hongwei Fang, Lu Zhao, Yonghu Chen, Chang-Kui Duan, and Min Yin. Optical thermometry of a Tm^{3+}/Yb^{3+} co-doped $LiLa(MoO_4)_2$ upconversion phosphor with a high sensitivity. *RSC Advances*, 6:84610–84615, 2016. doi: 10.1039/C6RA18432D. URL https://doi.org/10.1039/C6RA18432D.

S. D. Jackson and S. Mossman. Efficiency dependence on the tm^{3+} and al^{3+} concentrations for tm^{3+}-doped silica double-clad fiber lasers. *Applied Optics*, 42(15):2702–2707, 2003. doi: 10.1364/AO.42.002702. URL https://doi.org/10.1364/AO.42.002702.

D. Jaque and F. Vetrone. Luminescence nanothermometry. *Nanoscale*, 4:4301–4326, 2012. doi: 10.1039/C2NR30764B. URL https://doi.org/10.1039/C2NR30764B.

A.R. Jha, editor. *Rare Earth Materials: Properties and Applications*. Number 13:978-1-4665-6403-9 in Contemporary Mathematics. CRC Press, Taylor & Francis Group, 6000 Broken Sound Parkway NW, Suite 300, Boca Raton, FL, 2014.

Won Jin Kim, Marcin Nyk, and Paras N. Prasad. Color-coded multilayer photopatterned microstructures using lanthanide (iii) ion co-doped $NaYF_4$ nanoparticles with upconversion luminescence for possible applications in security. *Nanotechnology*, 20(18):185301, 2009. doi: 10.1088/0957-4484/20/18/185301. URL https://doi.org/10.1088/0957-4484/20/18/185301.

Y. Kim, P. Arunkumar, and B. Kim. A zero-thermal-quenching phosphor. *Nature Materials*, 16: 543–550, 2017. doi: 10.1038/nmat4843. URL https://doi.org/10.1038/nmat4843.

Phani Teja Kuruganti and Hairong Qi. Asymmetry analysis in breast cancer detection using thermal infrared images. In *Proceedings of the IEEE International Symposium on Biomedical Imaging*, pages 309–312, 2002. doi: 10.1109/ISBI.2002.1029255. URL https://doi.org/10.1109/ISBI.2002.1029255.

André S. Laia, Francisca J. R. Tavares, Matheus S. C. de Oliveira, Marcos V. dos S. Rezende, Iara de Fátima Gimenez, José J. Rodrigues Jr., and Márcio A. R. C. Alencar. Luminescent thermometry with YVO_4:Er/Nd: Achieving high sensitivities within the 1st and 2nd biological windows. *Journal of Luminescence*, 265:120239, 2023. doi: 10.1016/j.jlumin.2023.120239. URL https://doi.org/10.1016/j.jlumin.2023.120239.

André Scheidegger Laia, Daniela A. Hora, Marcos V. dos S. Rezende, Yutao Xing, José Joatan Rodrigues Jr., Glauco S. Maciel, and Márcio A.R.C. Alencar. Comparing the performance of Nd^{3+}-doped $LiBaPO_4$ phosphors as optical temperature sensors within the first biological window exploiting luminescence intensity ratio and bandwidth methods. *Journal of Luminescence*, 227:117524, 2020. doi: 10.1016/j.jlumin.2020.117524. URL https://doi.org/10.1016/j.jlumin.2020.117524.

Jianfu Li, Xiaoli Wang, and Zhankui Jiang. Multiphoton upconversion process in Tm^{3+}-doped ZBLAN glass by CW laser irradiation. *Optics Communications*, 282:4249–4251, 2009. doi: 10.1016/j.optcom.2009.06.067. URL https://doi.org/10.1016/j.optcom.2009.06.067.

Jingyun Li, Yuxiao Wang, Xueru Zhang, Liang Li, and Haoyue Hao. Up-converting luminescence and temperature sensing of $Er^{3+}/Tm^{3+}/Yb^{3+}$ co-doped $NaYF_4$ phosphors operating in the visible and the first biological window range. *Nanomaterials*, 11:2660, 2021. doi: 10.3390/nano11102660. URL https://doi.org/10.3390/nano11102660.

Z. Li, J. M. O. Daniel, Y. Jung, S. U. Alam, and D. J. Richardson. Thulium-doped fiber amplifier for optical communications at $2\mu m$. *Optics Express*, 21(8):9289–9297, 2013. doi: 10.1364/OE.21.009289. URL https://doi.org/10.1364/OE.21.009289.

Barbara A. Lindig, Michael A. J. Rodgers, and A. Paul Schaap. Determination of the lifetime of singlet oxygen in water-d_2 using 9,10-anthracenedipropionic acid, a water-soluble probe. *Journal of the American Chemical Society*, 102(17):5590–5593, 1980. doi: 10.1021/ja00537a030. URL https://doi.org/10.1021/ja00537a030.

Xiaofeng Liua and Jianrong Qiu. Recent advances in energy transfer in bulk and nanoscale luminescent materials: From spectroscopy to applications. *Chem. Soc. Rev.*, 44:8714–8746, 2015. doi: 10.1039/C5CS00067J. URL https://doi.org/10.1039/C5CS00067J.

Heike S. Mader, Peter Kele, Sayed M. Saleh, and Otto S. Wolfbeis. Upconverting luminescent nanoparticles for use in bioconjugation and bioimaging. *Current Opinion in Chemical Biology*, 14(5):582–596, 2010. doi: 10.1016/j.cbpa.2010.08.014. URL https://doi.org/10.1016/j.cbpa.2010.08.014.

L. Marciniak, K. Kniec, K. Elzbieciak-Piecka, K. Trejgis, J. Stefanska, and M. Draćicanin. Luminescence thermometry with transition metal ions. a review. *Coordination Chemistry Reviews*, 469:214671, 2022. doi: 10.1016/j.ccr.2022.214671. URL https://doi.org/10.1016/j.ccr.2022.214671.

M. Méndez, Y. Cesteros, L. F. Marsal, E. Martínez-Ferrero, P. Salagre, P. Formentín, J. Pallarès, M. Aguiló, F. Díaz, and J. J. Carvajal. Polymer composite $P3HT : Eu^{3+}$ doped La_2O_3 nanoparticles as a down-converter material to improve the solar spectrum energy. *Optical Materials*, 33(7):1120–1123, 2010. doi: 10.1016/j.optmat.2010.09.001. URL https://doi.org/10.1016/j.optmat.2010.09.001.

Jeevan M. Meruga, William M. Cross, P. Stanley May, QuocAnh Luu, Grant A. Crawford, and Jon J. Kellar. Security printing of covert quick response codes using upconverting nanoparticle inks. *Nanotechnology*, 23(39):395201, 2012. doi: 10.1088/0957-4484/23/39/395201. URL https://doi.org/10.1088/0957-4484/23/39/395201.

Chao Mi. *Ratiometric Nanothermometry Based on the Phonon-Assisted Anti-Stokes Luminescent Materials*. PhD thesis, University of Technology Sydney, 2019.

Qiuhong Min, Wenjuan Bian, Yushuang Qi, Wei Lu, Xue Yu, Xuhui Xu, Dacheng Zhou, and Jianbei Qiu. Temperature sensing based on the up-conversion emission of Tm^{3+} in a single $KLuF_4$ microcrystal. *Journal of Alloys and Compounds*, 728:1037–1042, 2017. doi: 10.1016/j.jallcom.2017.09.050. URL https://doi.org/10.1016/j.jallcom.2017.09.050.

W. J. Miniscalco. *Optical and electronic properties of rare earth ions in glasses*. Marcel Dekker Inc., New York, NY, 2001.

A. Nakatsuka, A. Yoshiasa, and S. Takeno. Site preference of cations and structural variation in $Y_3Fe_{5x}Ga_xO_{12}$ (0 x 5) solid solutions with garnet structure. *Acta Crystallographica Section B*, 51:737–745, 1995. doi: 10.1107/S0108768194014813. URL https://doi.org/10.1107/S0108768194014813.

Villads R. M. Nielsen, Maxime Grasser, Sabina Svava Mortensen, Boris Le Guennic, and Thomas Just Sorensen. Electronic structure of a neodymium(iii) tris(oxydiacetate) complex from luminescence data and ab initio calculations. *Inorg. Chem.*, 63(40):18596–18607, 2024. doi: 10.1021/acs.inorgchem.4c02242. URL https://doi.org/10.1021/acs.inorgchem.4c02242.

Kohki Okabe, Noriko Inada, Chie Gota, Yoshie Harada, Takashi Funatsu, and Seiichi Uchiyama. Intracellular temperature mapping with a fluorescent polymeric thermometer and fluorescence lifetime imaging microscopy. *Nature Communications*, 3:705, 2012. doi: 10.1038/ncomms1714. URL https://doi.org/10.1038/ncomms1714.

O. O. Oyebola, M. A. Olopade, and K. I. Ogungbemi. Infrared up-conversion emission observed in Ho^{3+}-doped potassium lead chloride. *Ilorin Journal of Science*, ILJS-15-022, 2015. doi: doi.org/10.54908/iljs.2016.03.02.006. URL https://doi.org/10.54908/iljs.2016.03.02.006.

Rajashree Panda, Mitrabhanu Behera, Mahesha Hegde, R. Arun Kumar, Gunasekaran Venugopal, Przemysław Woźny, Kevin Soler-Carracedo, and Marcin Runowski. High-sensitivity optical thermometer based on the luminescence of divalent and trivalent thulium ions in $CaAl_4O_7$ $:^{+2}$ Tm_{3+} operating in cryogenic and high temperature ranges. *Journal of Materials Chemistry C*, 13:8776–8791, 2025. doi: 10.1039/D4TC05342G. URL https://doi.org/10.1039/D4TC05342G.

P. S. Peijzel, A. Meijerink, R. T. Wegh, M. F. Reid, and G. W. Burdick. A complete $4f^n$ energy level diagram for all trivalent lanthanide ions. *Journal of Solid State Chemistry*, 178(2):448–453, 2005. doi: 10.1016/j.jssc.2004.07.046. URL https://doi.org/10.1016/j.jssc.2004.07.046.

Tingting Peng, Rui Pu, Baoju Wang, Zhimin Zhu, Kai Liu, Fan Wang, Wei Wei, Haichun Liu, and Qiuqiang Zhan. The spectroscopic properties and microscopic imaging of thulium-doped upconversion nanoparticles excited at different nir-ii light. *Biosensors*, 11:148, 2021. doi: 10.3390/bios11050148. URL https://doi.org/10.3390/bios11050148.

M. S. Pudovkin, S. L. Korableva, D. A. Koryakovtseva, E. V. Lukinova, A. V. Lovchev, O. A. Morozov, and V. V. Semashko. The comparison of Pr^{3+}:LaF_3 and Pr^{3+}:$LiYF_4$ luminescent nano- and microthermometer performances. *Journal of Nanoparticle Research*, 21:266, 2019. doi: 10.1007/s11051-019-4713-0. URL https://doi.org/10.1007/s11051-019-4713-0.

Hai Sheng Qian, Hui Chen Guo, Paul Chi-Lui Ho, Ratha Mahendran, and Yong Zhang. Mesoporous-silica-coated up-conversion fluorescent nanoparticles for photodynamic therapy. *Nano Micro Small*, 5(20):2285–2290, 2009. doi: 10.1002/smll.200900692. URL https://doi.org/10.1002/smll.200900692.

Patrick Rice and Bhaskar K. Somani. A systematic review of thulium fiber laser: Applications and advantages of laser technology in the field of urology. *Research and Reports in Urology*, 13:519–527, 2021. doi: 10.2147/RRU.S233979. URL https://doi.org/10.2147/RRU.S233979.

Rebecca Richards-Kortum and Eva Sevick-Muraca. Spectroscopy for tissue diagnosis. *Annu. Rev. Phys. Chem.*, 47:555–606, 1996. doi: 10.1146/annurev.physchem.47.1.555. URL https://doi.org/10.1146/annurev.physchem.47.1.555.

Joao Rocha, Carlos D. S. Brites, and Luís D. Carlos. Lanthanide organic framework luminescent thermometers. *Chemistry – A European Journal*, 22(42):14782–14795, 2016. doi: 10.1002/chem.201600860. URL https://doi.org/10.1002/chem.201600860.

Miguel Andrés Hernández Rodríguez. *Nanomaterials Doped with Lanthanide Ions under Extreme Conditions for Sensor and Photonics Applications*. PhD thesis, Universidad de La Laguna, 2018. URL http://riull.ull.es/xmlui/handle/915/25182.

Marcin Runowski, Przemysław Woźny, Natalia Stopikowska, Inocencio R. Martin, Víctor Lavín, and Stefan Lis. Luminescent nanothermometer operating at very high temperature—sensing up

to 1000 k with upconverting nanoparticles Tm^{3+}/Yb^{3+}. *ACS Applied Materials & Interfaces*, 12(39):43933–43941, 2020. doi: 10.1021/acsami.0c13011. URL https://doi.org/10.1021/acsami.0c13011.

A. M. Saad, Hanan Ali, P. Masschelein, H. Kabbara, Ahmed Asaad I. Khalil, I. M. Azzouz, and Alaa E. Giba. Infrared to visible upconversion photoluminescence from Nd-doped yttria ceramic for optical applications. *Braz. J. Phys.*, 53, 2023. doi: 10.1007/s13538-023-01303-y. URL https://doi.org/10.1007/s13538-023-01303-y.

Ol. A. Savchuk, J. J. Carvajal, J. Massons, C. Cascales, M. Aguiló, and F. Díaz. Novel low-cost, compact and fast signal processing sensor for ratiometric luminescent nanothermometry. *Sensors and Actuators A: Physical*, 250:87–95, 2016. doi: 10.1016/j.sna.2016.08.031. URL https://doi.org/10.1016/j.sna.2016.08.031.

Ol. A. Savchuk, J. J. Carvajal, J. Massons, C. Cascales, M. Aguiló, and F. Díaz. Luminescent nanothermometry using short-wavelength infrared light. *Journal of Alloys and Compounds*, 746: 710–719, 2018. doi: 10.1016/j.jallcom.2018.03.002. URL https://doi.org/10.1016/j.jallcom.2018.03.002.

Ol. A. Savchuk, J. J. Carvajal, C. Cascales, P. Haro-Gonzalez, F. Sanz-Rodriguez, M. Aguiló, and F. Díaz. Nir-to-nir upconversion emissions of Tm^{3+}/Yb^{3+}:$GdVO_4$@sio_2 core-shell nanoparticles for temperature sensing purposes and imaging in the first biological window. *Nanomaterials*, 10(5):993, 2020. doi: 10.3390/nano10050993. URL https://doi.org/10.3390/nano10050993.

T.K. Seshagiri, N.K. Porwal, V. Sudersan, A.K. Tyagi, and S.V. Godbole. Spectroscopic and luminescence studies of thulium doped strontium borate glass. *Journal of Non-Crystalline Solids*, 356(20–22):1032–1036, 2010. doi: 10.1016/j.jnoncrysol.2010.01.019. URL https://doi.org/10.1016/j.jnoncrysol.2010.01.019.

Nail M. Shavaleev, Rosario Scopelliti, Frederic Gumy, and Jean-Claude G. Bünzli. Modulating the near-infrared luminescence of neodymium and ytterbium complexes with tridentate ligands based on benzoxazole-substituted 8-hydroxyquinolines. *Inorg. Chem.*, 48(7):2908–2918, 2009. doi: 10.1021/ic8020468. URL https://doi.org/10.1021/ic8020468.

Flávia R.O. Silva, Nelson B. Lima, Walter K. Yoshito, Ana Helena A. Bressiani, and Laércio Gomes. Development of novel upconversion luminescent nanoparticles of ytterbium/thulium–doped beta tricalcium phosphate. *Journal of Luminescence*, 187:240–246, 2017. doi: 10.1016/j.jlumin.03.029. URL https://doi.org/10.1016/j.jlumin.2017.03.029.

David Allan Simpson. *Spectroscopy of Thulium-Doped Silica Glass*. PhD thesis, Victoria University, 2020.

R. G. Smart, J. N. Carter, A. C. Tropper, and D. C. Hanna. Lasing and amplification in the $0.8\ \mu m$ region in thulium-doped fluorozirconate fibers. *Electronics Letters*, 26(21), 1990. doi: 10.1049/el:19901130. URL https://doi.org/10.1049/el:19901130.

R. G. Smart, J. N. Carter, A. C. Tropper, D. C. Hanna, S. F. Carter, and D. Szebesta. 20 db gain thulium-doped fluorozirconate fibre amplifier operating at around $0.8\ \mu m$. *Electronics Letters*, 27(13), 1991. doi: 10.1049/el:19910701. URL https://doi.org/10.1049/el:19910701.

Andrew M. Smith, Michael C. Mancini, and Shuming Nie. Second window for in vivo imaging. *Nature Nanotechnology*, 4(11):710–711, 2009. doi: 10.1038/nnano.2009.326. URL https://doi.org/10.1038/nnano.2009.326.

J. García Solé, L.E. Bausá, and D. Jaque, editors. *An Introduction to the Optical Spectroscopy of Inorganic Solids*. John Wiley & Sons, The Atrium, Southern Gate, Chichester, West Sussex PO19 8SQ, England, 2005. ISBN 0-470-86886-4.

Adam Strzepek, Michał Głowacki, Maksymilian Szatko, Karolina Potrzebska, Witold Ryba-Romanowski, and Radosław Lisiecki. Spectroscopic properties of thulium doped $(Lu_{0.25}Gd_{0.75})_2SiO_5$ (LGSO) single crystals. *Journal of Luminescence*, 220:116962, 2020. doi: 10.1016/j.jlumin.2019.116962. URL https://doi.org/10.1016/j.jlumin.2019.116962.

Hao Suo, Fangfang Hu, Xiaoqi Zhao, Zhiyu Zhang, Ting Li, Changkui Duan, Min Yin, and Chongfeng Guo. All-in-one thermometer-heater up-converting platform YF_3:Tm^{3+}/Yb^{3+} operating in the first biological window. *J. Mater. Chem. C*, 5:1501–1507, 2017. doi: 10.1039/C6TC05449H. URL https://doi.org/10.1039/C6TC05449H.

Wenyan Tian and B. Rami Reddy. Ultraviolet upconversion in thulium-doped fluorozirconate fiber observed under two-color excitation. *Optics Letters*, 26(20):1580–1582, 2001. doi: 10.1364/OL.26.001580. URL https://doi.org/10.1364/OL.26.001580.

A. Tropper, R. Smart, I. Perry, D. Hanna, J. Lincoln, and B. Brocklesby. Thulium-doped silica fiber lasers. In *Fiber Laser Sources and Amplifiers II, Proc. SPIE, Vol. 1373*, 1991. doi: 10.1117/12.24937. URL https://doi.org/10.1117/12.24937.

Madan M. Upadhyay, Kumar Shwetabh, and Kaushal Kumar. Comparative studies of upconversion luminescence and optical sensing in Tm^{3+}/Yb^{3+} co-doped $LaVO_4$ and $GdVO_4$ phosphors. *RSC Advances*, 13:20674–20683, 2023. doi: 10.1039/D3RA03273F. URL https://doi.org/10.1039/D3RA03273F.

P. A. Usachev, R. V. Pisarev, A. M. Balbashov, A. V. Kimel, A. Kirilyuk, and Th. Rasing. Optical properties of thulium orthoferrite $TmFeO_3$. *Phys. Solid State*, 47:2292–2298, 2005. doi: 10.1134/1.2142893. URL https://doi.org/10.1134/1.2142893.

F. Vetrone, R. Naccache, A. Zamarrón, A.J. De La Fuente, L.M. Maestro, E.M. Rodriguez, D. Jaque, J.G. Sole, and J.A. Capobianco. Temperature sensing using fluorescent nanothermometers. *ACS Nano*, 4:3254–3258, 2010. doi: 10.1021/nn100244a. URL https://doi.org/10.1021/nn100244a.

J.H.L. Voncken, editor. *The Rare Earth Elements: An Introduction*. SpringerBriefs in Earth Sciences, Delft, The Netherlands, 2016. ISBN 978-3-319-26807-1. doi: 10.1007/978-3-319-26809-5.

S. A. Wade, S. F. Collins, and G. W. Baxter. Fluorescence intensity ratio technique for optical fiber point temperature sensing. *Journal of Applied Physics*, 94:4743–4756, 2003. doi: 10.1063/1.1606526. URL https://doi.org/10.1063/1.1606526.

B. M. Walsh and N. P. Barnes. Comparison of tm:zblan and tm: silica fiber lasers; spectroscopy and tunable pulsed laser operation around $1.9\ \mu m$. *Journal of Applied Physics B*, 78:325–333, 2004. doi: 10.1007/s00340-003-1393-2. URL https://doi.org/10.1007/s00340-003-1393-2.

Chao Wang, Liang Cheng, and Zhuang Liu. Upconversion nanoparticles for photodynamic therapy and other cancer therapeutics. *Theranostics*, 5:317–330, 2013a. doi: 10.7150/thno.5284. URL https://doi.org/10.7150/thno.5284.

Shuxian Wang, Hengjiang Cong, Kui Wu, Zhongben Pan, Haohai Yu, Junhai Liu, Robert I. Boughton, and Huaijin Zhang. Composition characterization in YSGG garnet single crystals for ytterbium laser. *Optical Materials Express*, 3:1408, 2013b. doi: 10.1364/OME.3.001408. URL https://doi.org/10.1364/OME.3.001408.

Weiqing Wu, Yurong Xu, Xinyi Lin, Fazheng Huang, Ya-Nan Feng, Lizhen Zhang, Yan Yu, and Lingyun L. Ultra-stable Er^{3+}/Yb^{3+} co-doped scheelite single crystals for wide-range fiber-free optical thermometry. *Journal of Luminescence*, 283:121251, 2025. doi: 10.1016/j.jlumin.2025.121251. URL https://doi.org/10.1016/j.jlumin.2025.121251.

Arepati Xiakeer, Lin-Xiang Wang, Qing Li, Yun-Feng Bai, and Munire Maimaiti. Preparation and temperature sensing properties of Tm^{3+}/Yb^{3+} co-doped Bi_2WO_6 upconversion luminescent materials. *Acta Physica Sinica*, 72(6):060701, 2023. doi: 10.7498/aps.72.20222143. URL https://doi.org/10.7498/aps.72.20222143.

Zhisong Xiao, R. Serna, Fei Xu, and C. N. Afonso. Critical separation for efficient Tm^{3+}–Tm^{3+} energy transfer evidenced in nanostructured Tm^{3+}:Al_2O_3 thin films. *Optics Letters*, 33(6): 608–610, 2008. doi: 10.1364/ol.33.000608. URL https://doi.org/10.1364/OL.33.000608.

Lu Yu, Linhua Ye, Renjie Bao, Xianwei Zhang, and Li-Gang Wang. Sensitivity-enhanced Tm^{3+}/Yb^{3+} co-doped YAG single crystal optical fiber thermometry based on upconversion emissions. *Optics Communications*, 410:632–636, 2017. doi: 10.1016/j.optcom.2017.10.075. URL https://doi.org/10.1016/j.optcom.2017.10.075.

T. Zdanowlcz. Electrical properties of thulium oxide thin films. *Thin Solid Films*, 164:175–182, 1988. doi: 10.1016/0040-6090(88)90130-7. URL https://doi.org/10.1016/0040-6090(88)90130-7.

Huiting Zhang, Zhonghua Zhu, Shengdi Ta, Ninghan Zeng, Peng Zhang, Limin Wu, Shoulei Xu, Bernard Albert Goodman, and Wen Deng. Highly efficient orange-red emission in Sm^{3+}-doped yttrium gallium garnet single crystal. *Crystals*, 13:1273, 2023. doi: 10.3390/cryst13081273. URL https://doi.org/10.3390/cryst13081273.

Qifan Zhang, Juan Kong, Shanshan Ye, Kan Lu, Yan Hao, Wenxia Wu, Guozhu Xiong, Yazhao Wang, Shoulei Xu, and Wen Deng. Highly efficient up- and down-conversion photoluminescence in er/tm/yb co-doped lutecia-stabilized zirconia single crystals. *Journal of Alloys and Compounds*, 1008:176551, 2024. doi: 10.1016/j.jallcom.2024.176551. URL https://doi.org/10.1016/j.jallcom.2024.176551.

Jiajia Zhou, Shihui Wen, Jiayan Liao, Christian Clarke, Sherif Abdulkader Tawfik, Wei Ren, Chao Mi, Fan Wang, and Dayong Jin. Activation of the surface dark-layer to enhance upconversion in a thermal field. *Nature Photonics*, 12:154–158, 2018. doi: 10.1038/s41566-018-0108-5. URL https://doi.org/10.1038/s41566-018-0108-5.

6. Appendix

6.1 Excitation power variation

Fitting parameters and uncertainties with potential variation in the NIR infrared region under 800nm

		Value	Standard Error
1650nm	Intercept	3.03474	0.01246
	Slope	0.92744	0.00895
1050 nm	Intercept	2.56019	0.01449
	Slope	0.90682	0.01041
1450 nm	Intercept	1.90673	0.012
	Slope	0.94078	0.008620

Table 6.1: Fitting parameters and uncertainties of 4.12

Fitting parameters and uncertainties with potential variation in the visible range under 980nm

		Value	Standard Error
485nm	Intercept	-1.40335	0.05246
	Slope	2.68379	0.03388
650 nm	Intercept	-1.60457	0.023871
	Slope	2.76276	0.015417
685 nm	Intercept	0.74626	0.04903
	Slope	1.92479	0.03167

Table 6.2: Fitting parameters and uncertainties of 4.11

Fitting parameters and uncertainties with potential variation in the NIR infrared region under 980nm

		Value	Standard Error
1650nm	Intercept	2.96436	0.01612
	Slope	0.90207	0.01041
1450 nm	Intercept	1.3458	0.01316
	Slope	1.2208	0.0085

Table 6.3: Fitting parameters and uncertainties of 4.13

Fitting parameters and uncertainties with potential variation in the visible range under 980nm

		Value	Standard Error
485nm	Intercept	-2.39366	0.013677
	Slope	2.38076	0.06308
650 nm	Intercept	-0.01554	0.02799
	Slope	1.71859	0.01291
685 nm	Intercept	-2.27385	0.325
	Slope	2.28109	0.1488

Table 6.4: Fitting parameters and uncertainties of 4.10

6.2 Temperature variation

The Fitting parameters of I_{1650}/I_{1450} under 800 nm.

		Value	Standard Error
Mean	y0	158.14388	234.38481
	A	-178.8656	226.53507
	R	-7.17934E-4	0.00119

Table 6.5: Fitting parameters and uncertainties of 4.19

The Fitting parameters of ratio I_{1650}/I_{1050} under 800 nm.

		Value	Standard Error
Mean	Intercept	-6.01972	0.03908
	Slope	0.0305	1.21312E-4

Table 6.6: Fitting parameters and uncertainties of 4.18

The Fitting parameters of ratio I_{1650}/I_{1450} under 980 nm.

		Value	Standard Error
Mean	y0	2.32721	5.12017
	A	1.95753	1.04179
	R	0.00879	0.00117

Table 6.7: Fitting parameters and uncertainties of 4.20

The Fitting parameters of ratio I_{685}/I_{485} under 980 nm.

		Value	Standard Error
Mean	y0	9.01838	1.38404
	A	5.07484E-4	0.00144
	R	0.02734	0.00749

Table 6.8: Fitting parameters and uncertainties of 4.24

The Fitting parameters of ratio I_{685}/I_{650} under 980 nm excitation.

		Value	Standard Error
Mean	y0	5.746	0.41789
	A	0.0021	0.00202
	R	0.0215	0.00231

Table 6.9: Fitting parameters and uncertainties of 4.23

The Fitting parameter of ratio I_{685}/I_{485} under 800 nm excitation.

		Value	Standard Error
Mean	y0	2.4114	4.28042
	A	0.01013	0.001584
	R	0.02351	0.00411

Table 6.10: Fitting parameters and uncertainties of 4.22

The Fitting parameter of ratio I_{685}/I_{650} under 800 nm excitation.

		Value	Standard Error
Mean	y0	-2.73927	3.85986
	A	0.14242	0.011989
	R	0.01585	0.00280

Table 6.11: Fitting parameters and uncertainties of 4.21